

Long-term Pannexin 1 Ablation Produces an Imbalance Between Small Rho-GTPases Activity and Actin Polymerization Leading to Structural and Functional Modifications in Hippocampal Neurons

Carolina Flores-Muñoz

Universidad de Valparaíso

Francisca García-Rojas

Universidad de Valparaíso

Miguel A. Perez

Universidad de Valparaíso

Odra Santander

Universidad de Valparaíso

Elena Mery

Universidad de Valparaíso

Daniela Lopez-Espíndola

Universidad de Valparaíso

Arlek M. Gonzalez-Jamett

Universidad de Valparaíso

Marco Fuenzalida

Universidad de Valparaíso

Agustín D. Martinez

Universidad de Valparaíso

Alvaro Oscar Ardiles (✉ alvaro.ardiles@uv.cl)

Universidad de Valparaíso <https://orcid.org/0000-0001-8295-2133>

Research Article

Keywords: Pannexin1, actin cytoskeleton, Rho GTPases, neuronal morphology, dendritic spines, hippocampal neurons

Posted Date: January 12th, 2022

DOI: <https://doi.org/10.21203/rs.3.rs-1242197/v1>

License:  This work is licensed under a Creative Commons Attribution 4.0 International License.

[Read Full License](#)

Abstract

Enhanced activity and overexpression of Pannexin 1 (PANX1) channels contribute to neuronal pathologies, such as epilepsy and Alzheimer's disease (AD). In the hippocampus, the PANX1 channel ablation alters glutamatergic neurotransmission, synaptic plasticity, and memory flexibility. Nevertheless, PANX1-knockout (PANX1-KO) mice still preserve the ability to learn, suggesting that compensatory mechanisms work to stabilize neuronal activity. Here, we show that the absence of PANX1 in the adult brain promotes a series of structural and functional modifications in PANX1-KO CA1 hippocampal synapses, preserving spontaneous activity. Adult CA1 neurons of PANX1-KO mice exhibit enhanced excitability, a more complex dendritic branching, enhanced spine maturation, and multiple synaptic contacts compared to the WT condition. These modifications seem to rely on the actin-cytoskeleton dynamics as an increase in actin polymerization and an imbalance between Rac1 and RhoA GTPase activity is observed in the absence of PANX1. Our findings highlight a novel interaction between PANX1, actin, and small Rho GTPases, which appear to be relevant for synapse stability.

Introduction

PANX1 is a heptameric channel that enables the movement of ions and small molecules between intracellular and extracellular compartments, contributing to the paracrine communication in mammalian cells [1-5]. PANX1 channels exhibit two modes of activity with different properties of ion and solute permeability [6]. At negative potentials, PANX1 channels show a constitutive small pore ion channel activity characterized by low conductance, slightly anion selectivity (chloride ions) and outwardly rectifying currents [7-10], while at depolarizing potentials, these channels exhibit a large pore conformation with high conductance mediating a non-selective ionic flux responsible for the permeation of ATP, and other metabolites. ATP released by PANX1 channels is triggered by intense or chronic neuronal activity [11,12], high concentrations of external potassium [13], mechanical stress [14], low oxygen conditions [15,16], ionotropic and metabotropic receptor signaling (NMDAR [11,17], P2X7R [18], α 1AR [19], α 7-nAChR[20], and caspase-dependent cleavage of its carboxy-terminal [21,22]. However, it remains unclear the precise contribution of PANX1 to neuronal function under resting activity.

Aberrant PANX1 activity has been implicated in several conditions affecting the central nervous system (CNS) [23,4], including ischemia [24,25], epilepsy [26-28], and Alzheimer's disease [29]. Nevertheless, PANX1 channels also mediate physiological processes in the brain. In the adult mouse brain, PANX1 absence or blockade increases the excitatory synaptic transmission and modifies the induction of synaptic plasticity [30,31]. Furthermore, during embryonic and early postnatal development, PANX1 ablation promotes neurite outgrowth, dendritic spine development, and network assembly [32,33]. Thus, the fine regulation of PANX1 activity and expression could be a critical aspect for the proper functioning of neurons, as well as for the brain circuit formation. In this regard, it is intriguing to know the long-term effect of PANX1 ablation on both processes underlying structural plasticity.

It is known that the polarized and highly branched morphology of neurons is crucial to establishing synaptic contacts and hence neural circuits. In fact, plastic changes in neuronal circuits are believed to be the basis of high-order brain functions such as cognition [34], and perturbations in their regulation are associated with synaptopathies [35]. Most of the excitatory synapses are localized on dendritic spines, highly dynamic structures exhibiting the capacity to change their morphology and density in response to neural activity [36]. Thus, the synapses are constantly subjected to activity-dependent plasticity to store information. Consequently, they are simultaneously compensated to avoid instability in the circuits preserving their plasticity and cognitive abilities. In this regard, homeostatic regulatory changes occur at the cell and circuit level to adapt neural properties and their molecular components to provide a balanced control of synaptic strength [37]. Several mechanisms have been reported, such as metaplasticity, synaptic scaling, and intrinsic plasticity (for review, see [38-41]), which can be executed through a variety of cellular and molecular processes depending on the development state and neuronal activity [42]. Previously, it was reported that the lack of PANX1 activity in the adult hippocampus produces metaplastic changes modifying the threshold for induction of excitatory LTP and LTD [30]. However, this change was revealed under activity demand, and it is unknown whether PANX1 ablation elicits additional modifications to preserve neuronal activity at resting conditions. Interestingly, a recent study reported that early postnatal PANX1 ablation prevents the homeostatic adjustment of presynaptic strength upon chronic inactivity [43].

Here, we show that PANX1 deletion (PANX1-KO) in the adult mouse brain promotes several changes in the excitability and synaptic transmission as well as extensive structural modifications in CA1 hippocampal neurons. PANX1-KO CA1 neurons exhibited enhanced excitability, higher dendritic arborization and spine maturation, as well as increased size of the readily releasable pool (RRP) compared to the wild-type (WT) condition. Furthermore, they exhibited an increased size of the postsynaptic density (PSD), and an increased number of synaptic contacts at the ultrastructural level, although, the estimation of a multiplicity-index revealed that the release sites or functional contacts were lower in PANX1-KO neurons. Remarkably, such modifications correlated with perturbations in the actin cytoskeleton dynamics, as was observed enhanced expression of the actin-related proteins, higher expression of the activated form of the small Rho-GTPase Rac1, and augmented F-actin content in hippocampal tissue of PANX1-KO mice. Altogether, our data strongly suggest that PANX1 plays a “stabilizing” role in the neuronal function and morphology by modulating actin dynamics, through a mechanism that involves the small-Rho-GTPase family.

Materials And Methods

Animals

The experiments were carried out in adult homozygous male (6-9 months old) C57BL/6 or PANX1-KO mice. The generation of PANX1-KO mice has been described previously [44]. Mice were maintained at $21 \pm 1^\circ\text{C}$, at constant humidity (55%) and in a 12/12 h dark-light cycle; with a light phase from 08:00 to

20:00, food and water were provided *ad libitum*. All animal experiments were approved by the Institutional Animal Care and Use Committee of the Universidad de Valparaiso (BEA064-2015 and BEA160-2020).

Electrophysiology

Animals were deeply anesthetized with isoflurane (Forane, B506, AbbVie, IL, USA), the brains were quickly removed and submerged in a cold (4°C) dissection buffer (in mM: 124 sucrose, 2.69 KCl, 1.25 KH₂PO₄, 10 MgSO₄, 26 NaHCO₃, 10 glucose). Then, coronal hippocampal slices (350 μm) were cut with a Vibratome (WPI Instruments, model NVSLM1, FL, USA) and maintained for > 1 h at room temperature (20°C) in artificial cerebrospinal fluid (ACSF) composed, in mM: 124 NaCl, 2.69 KCl, 1.25 KH₂PO₄, 2 MgSO₄, 26 NaHCO₃, 2 CaCl₂, and 10 glucose. The pH of the dissection buffer and ACSF were adjusted at 7.4 with NaOH or HCl and stabilized by bubbling carbogen (95% O₂, 5% CO₂). To perform electrophysiological recordings, the slices were transferred into a 2 mL chamber fixed to an upright Nikon Eclipse FN1 microscope stage (Nikon Instruments, TYO, JP) equipped with infrared differential interference contrast (DIC) video microscopy and a 40X water immersion objective. The slices were continuously perfused with carbogen bubbled ACSF (2 mL/min) and maintained at room temperature (22-24°C). Picrotoxin (PTX; 10 mM, Tocris, PA, USA) and tetrodotoxin (TTX; 0.5 mM, Cayman Chemical (FL, USA)) were added to the ACSF as needed. Whole-cell recordings were performed from the soma of pyramidal neurons from the CA1 area of vHPC with patch pipettes (4–8 MW) filled with an internal solution containing, in mM: 131 Cs-Gluconate, 10 HEPES, 10 EGTA, 4 Mg²⁺-ATP, 2 Glucose, 1 CaCl₂, 8 NaCl and 0.4 Na₃GTP, buffered to pH 7.2–7.3 with CsOH or 97.5 K⁺ Gluconate, 32.5 KCl, 5 EGTA, 1 MgCl × 6 H₂O and 10 HEPES, adjusted to pH 7.2–7.3 with KOH as needed. Recordings were performed in a voltage-clamp configuration using an EPC-7 patch-clamp amplifier (HEKA Instruments, MA, USA). The holding potential (V_h) was adjusted to -65 mV to record excitatory postsynaptic currents (EPSCs). In the voltage-clamp configuration, the series resistance was compensated to ~70%, and neurons were accepted only when the seal resistance was > 1 GW, and the series resistance (7–14 MW) did not change by > 20% during the experiment. The liquid junction potential was measured (~6 mV) but not corrected. Voltage-clamp data were low-pass filtered at 3.0 kHz and sampled at rates between 6.0 and 10.0 kHz using an A/D converter (ITC-16, InstruTech, MA, USA) and stored with the Pulse FIT software (HEKA, Instruments, MA, USA). The Pulse Fit program was used to generate stimulus timing signals and transmembrane current pulses. The recording analysis was made offline with pClamp software (Clamp-fit, Molecular Devices, CA, USA). eEPSCs were evoked by stimulation in Schaffer collaterals and recording in *Stratum pyramidale*. Stimulation was made with septate pipette containing two silver wires coupled to a stimulation source (Isoflex, AMPI, JRS, IL) and it was filled with ACSF. The stimulation electrode was positioned at ~50 μm from the recording pipette. Averages of EPSCs were obtained by repeated stimulation at 0.3 Hz. We evaluated two forms of short-term synaptic plasticity: paired-pulse ratio and use-dependent depression. Paired-pulse stimulus was applied at four different intervals (30, 70, 100, and 300 ms) and was calculated as R₂/R₁, where R₁ and R₂ correspond to peak amplitudes of the first and second synaptic response, respectively. Six to ten responses at each intensity were averaged to compute the EPSC amplitude. sEPSC recordings were continuously recorded at -65 mV for 30 min, under PTX. In addition, mEPSCs were recorded after adding

the voltage-gated sodium channel blocker, TTX (0.5 mM), to the bath. To estimate the size of the readily releasable pool of vesicles, we use an approximation as previously described [45-47]. Use-dependent synaptic depression was analyzed using 14 Hz bursts of 25 stimuli every 60 s (~3 V, 200 ms). The amplitudes of EPSCs evoked by the train were measured and summed, and a graph was made of the cumulative EPSC. Finally, multiplicity was estimated as previously described [48,49]. Multiplicity index was calculated as the mean amplitude of action potential-driven events (a) divided by mean quantal size (q: mean amplitude of mEPSC recorded in TTX). The (a) values were determined for each cell, subtracting the contribution of mEPSC to the pool of events collected in the absence of TTX, using the expression for a:

$$a = \frac{f_b b - f_q q}{f_b - f_q}$$

(1)

Where f_b and f_q denote the mean frequency values from events recorded before and after the addition of TTX to the perfusion media, respectively, and (b) is the mean amplitude of both action-potential-driven sEPSC and mEPSC.

For extracellular field recordings, transverse hippocampal slices (350- μ m-thick) were dissected in ice-cold (4°C) dissection buffer, in mM: 212.7 sucrose, 2.6 KCl, 1.23 NaH₂PO₄, 26 NaHCO₃, 10 dextrose, 3 MgCl₂, and 1 CaCl₂, using a vibratome (Leica VT1200S, Leica Microsystems, BW, GE). Slices then were recovered for 1 h at room temperature in ACSF, in mM: 124 NaCl, 5 KCl, 1.25 NaH₂PO₄, 26 NaHCO₃, 10 glucose, 1.5 MgCl₂, and 2.5 CaCl₂. Both dissection buffer and ACSF were pH adjusted at 7.4 and bubbled with carbogen (95% O₂, 5% CO₂). After recovery, the slices were placed in a submersion recording chamber perfused with ACSF (28 \pm 0.5°C; 2 mL/min). Field excitatory postsynaptic potentials (FPs), basically AMPAR-mediated FPs (AR-FPs), were evoked by stimulating Schaffer collaterals with 0.2 ms pulses delivered through concentric bipolar stimulating electrodes (FHC Inc., ME, USA) and recorded in CA1 *Stratum radiatum* using glass electrodes filled with ACSF (1 M Ω). FPs were amplified, low-pass filtered (1700 Differential AC Amplifier, A-M Systems, WA, USA), and then digitized (NI PCI-6221; National Instruments, TX, USA) for measurement. Baseline responses were recorded at 0.033 Hz. Next, NMDAR EPSPs (NR-FP) were isolated by applying CNQX (10 mM, Tocris, PA, USA) in ACSF containing 2 mM calcium and 0.1 mM magnesium. After 30 min of CNQX pre-incubation, NR-FPs were recorded. Finally, basal synaptic transmission was assayed by determining input-output relationships from FPs generated by gradually increasing the stimulus intensity; the input was the peak amplitude of the fiber volley (FV), and the output was the initial slope of FP. Data were monitored, analyzed online, and reanalyzed offline using a homemade program based on Igor software (Wavemetrics, OR, USA). Representative traces are an average of four consecutive responses.

Golgi staining to dendritic morphology visualization.

Neuron morphology and dendritic spines were measured using the FD Rapid GolgiStain Kit according to the manufacturer's guidelines (FD NeuroTechnologies, MD, USA). Briefly, dissected mouse brains were immersed in Solution A/B for two weeks at room temperature in dark conditions. Next, brains were placed in Solution C for 24 h in the dark. Afterward, coronal slices 150 μm thick were obtained using a semi-automatic cryostat microtome (Kedee KD-2950, ZJ, CN) at -20°C and mounted on gelatin-coated microscope slides with Solution C. The sections were allowed to dry naturally at room temperature, then placed in a mixture of Solution D/E for 10 min. Next, sections were rinsed twice in Milli-Q water for 4 min each time. Finally, the sections were dehydrated, cleared in xylene, and mounted using Permount mounting media (Sigma-Aldrich, MA, USA).

Morphometric analysis

For morphometric analysis, digital images were taken of individual well-impregnated pyramidal neurons of the CA1 region using a Leica DM500 microscope (Leica Microsystems Inc., IL, USA) equipped with a 40X objective, and ICC50W digital camera (Leica Microsystems Inc., IL, USA). Neurons were then drawn with the aid of a camera lucida (Leica drawing device L3/20) attached to the microscope (Leica Microsystems Inc., IL, USA) and digitalized in 1.200×1.200 dpi resolution to morphometric Sholl analysis using the Neuroanatomy and Simple neurite tracer plugins of Fiji software. In short, a series of concentric spheres (centered around the soma) were drawn with an intersection interval of 20 μm to calculate the number of dendrites crossing each sphere. This analysis was done for basal and apical dendrites and was plotted against the distance from the soma. Three parameters were used to determine dendritic morphology and complexity: 1) the number of dendrites; 2) the total dendritic length, including all dendritic branches; 3) the number of dendritic branches; and 4) the branch order. All morphological analysis were performed blind to the experimental conditions.

For spines analysis, dendritic segments from primary and secondary branches of 10 to 20 μm in length were selected randomly. Images were acquired using a Leica DM500 microscope (Leica Microsystems Inc., IL, USA) equipped with a 63X oil HCPL APO objective (NA 1.40) and ICC50w digital camera (Leica Microsystems Inc., IL, USA). Spine density was defined as the number of spines per 10 μm . Dendritic spines were classified according the following parameters [50]: Long, thin without-head protrusions of more than 2 μm long were classified as immature filopodia; wide-head (>0.6 μm width) and short protrusions (<1 μm) were classified as mature mushroom-spines; wide-head/without neck protrusions (length: width ratio <1 μm) were classified as stubby-spines; thin and short (<2 μm) headed protrusions were classified as thin-spines. Cup-shaped protrusions were classified as branched spines. The spines parameters were analyzed using Image J (version 1.49v; NIH, USA).

Electron Microscopy on hippocampal CA1 region

Electron microscopy analysis was performed for histological studies as previously reported [51]. Mice were transcardially perfused with a mixture of 4% PFA and 0.5% glutaraldehyde, followed by post-fixation in the same mixture ON at 4°C . Brain tissue blocks were trimmed in the CA1 area of the hippocampus and dehydrated in a graded series of ethanol, infiltrated in 1:1 volumes of 100% ethanol and 100% LR White

(EMS) during 4 h, immersed in 1.5% OsO₄ in 0.1 M sodium phosphate buffer (pH 7.4) for 2 h and then embedded in epoxy resin which was polymerized at 50°C ON. Ultrathin sections (90 nm) were made using an ultramicrotome (Leica Ultracut R, Leica Microsystems, ZQQ, GE) and contrasted with 1% uranyl acetate and lead citrate and located on nickel 300 mesh grids (Ted Pella Inc., CA, USA). Grids were observed under a transmission electron microscope Philips Tecnai 12 operated at 80 kV (FEI/Philips Electron Optics, EIN, NL) equipped with a digital micrograph Megaview G2 CCD camera (Olympus-SIS, MU, GE). Synapses from 1 littermate pair have been analyzed by an experimenter who was blind to the genotype, and the following parameters were analyzed: total number of synaptic vesicles, number of docked vesicles, number of vesicles within the active zone, PSD length, and number of synaptic contacts.

Subcellular fractionation-Synaptoneurosome isolation.

Synaptoneurosomes were extracted from the hippocampus of 6 m.o adult male mice as we previously reported [51]. Hippocampi were homogenized using a Dounce Tissue Grinder in ice-cold homogenization buffer containing, in mM: 320 sucrose, 4 HEPES, 1 EGTA, and protease and phosphatase inhibitor's cocktail buffered to pH 7.4. The homogenate was centrifuged at 1,800 rpm at 4°C for 10 min (Beckman F0630 rotor, IN, USA) obtaining a supernatant (S1) which was collected whereas the pellet (P1) was discarded. Then, S1 was centrifuged at 30,000 rpm at 4°C for 30 min (Beckman S4180 rotor, IN, USA). The obtained pellet (P2) containing the membrane proteins was re-suspended in homogenization buffer, layered on the top of a discontinuous sucrose density gradient (0.32/1.0/1.2 M) and subjected to ultracentrifugation at 86,000 rpm (Beckman SW-60ti rotor, IN, USA) at 4°C for 2 h. Afterwards, both the sediment and sucrose 0.32/1M interface were discarded, whereas material accumulated at the interface of 1.0 M and 1.2 M sucrose containing synaptoneurosome fraction was collected (SP1). SP1 was diluted with lysis buffer to restore the sucrose concentration back to 320 mM and remained on ice with gently agitation for 30 min. Then, SP1 was centrifuged at 30,000 rpm for 30 min. The pellet obtained (PS1) was resuspended in a gradient loading buffer, loaded on 0.32/1.0/1.2 M discontinuous gradient, and centrifuged at 86,000 rpm for 2 h. The sucrose 1/1.2M interphase, synaptoneurosome fraction 2 (SP2), was recovered and delipidated in a delipidating buffer. Next, SP2 was diluted with a filling buffer to restore the sucrose concentration and then centrifuged at 30,000 rpm for 1 h. The sediment obtained (PS2) was washed with 50 mM HEPES-Na and centrifuged at 86,000 rpm for 20 min. The final sediment obtained (PS3), containing postsynaptic densities (PSDs), was re-suspended in 50 mM HEPES-Na and homogenized. PS2 or PSD fractions were quantified for protein concentration using the Qubit® Protein Assay Kit (Thermo Scientific IL, USA).

Immunoblotting

Total proteins and synaptosomal fractions were processed for western blotting as previously described [52]. Samples for total tissue proteins were homogenized in ice-cold lysis buffer containing: 150 mM NaCl, 10 mM Tris-Cl, pH 7.4, EDTA 2 mM, 1% Triton X-100 and 0.1% SDS, supplemented with a protease and phosphatase inhibitor cocktail (Thermo Scientific, IL, USA) using a Potter-homogenizator. Protein samples were centrifuged twice for 5 min at 14,000 rpm. (4°C). Protein concentration was

determined using the Qubit® Protein Assay Kit (Thermo Scientific IL, USA). For both cases, 40 µg of protein per lane were resolved by 10% SDS-PAGE, and 12% SDS-PAGE for actin-proteins followed by immunoblotting on PVDF membranes (BioRad, California, USA) and probe with specific antibodies against Panx1 (rabbit anti-Panx1, ABN242 Merck; 1:1000), PSD95 (mouse anti-PSD95, MAB1596 Merck; 1:1000), SAP102 (mouse anti-SAP102, NeuroMAP; 1:500), Synaptophysin (goat anti-SYP, sc-91116 Santa Cruz; 1:2000), Syntaxin (rabbit anti-STX, sc-5899 Santa Cruz; 1:1000), Arp3 (rabbit anti-Arp3, 07272 Merck; 1:1000), N-WASP (mouse anti-N WASP, Santa Cruz; 1:2000), Rac1 (mouse anti-Rac1, sc-217 Santa Cruz; 1:1000), RhoA (mouse anti-RhoA, sc-418 Santa Cruz; 1:1000), Cdc42 (mouse anti-Cdc42, sc-8401 Santa Cruz; 1:1000) and GAPDH (mouse anti-GAPDH, sc-47724, Santa Cruz; 1:1000). After primary antibody incubation and washing, incubation with a secondary anti-mouse HRP antibody (1:5000), anti-rabbit HRP antibody (1:5000) or with anti-goat HRP antibody (1:5000) was performed for 1 h. Finally, western blot was developed by chemiluminescence using ECL (Pierce, Thermo Scientific, IL, USA). Immunoreactive bands were scanned and densitometrically quantified using the Image J software (version 1.49v; NIH, MD, USA). Total and synaptosomal fractions proteins data were normalized to GAPDH and expressed as a % of the WT samples.

Rho GTPases activation assay

Hippocampal slices were stabilized in a chamber with oxygenated (95% O₂ and 5% CO₂) ACSF at pH 7.4 for 1 h. The GTP loading of Rac1, Cdc42, and RhoA was measured using a Rho GTPase Activation Assay Combo Biochem Kit (BK030, Cytoskeleton Inc., CO, USA), according to the manufacturer's recommendations. Briefly, the hippocampal lysates were incubated at 4°C on a rocker for 1 h with Rac/Cdc42 (PAK1 PAK-binding domain) or RhoA (Rhotekin-binding domain) beads which binds specifically to GTP-bound, and not GDP-bound. Agarose beads were collected by centrifugation (for 3 min at 5,000 g at 4°C), washed and the immunoprecipitated resolved on 12% SDS-PAGE and detected via Western blot analysis using Cdc42 (mouse anti-Cdc42, ACD03 Cytoskeleton; 1:250), Rac1 (mouse anti-Rac1, ARC03 Cytoskeleton Inc; 1:500) and RhoA (mouse anti-RhoA, ARH05 Cytoskeleton Inc; 1:500), and visualized by ECL (Pierce, Thermo Scientific, IL, USA). Densitometric analysis was performed using the Image J software (version 1.49v; NIH, MD, USA). The Rac/Cdc42 or RhoA activation values were expressed as the ratio of Rac1-GTP, Cdc42-GTP, or RhoA-GTP against the total of proteins of each RhoGTPases in the crude extract.

F-actin quantification

Hippocampal slices were fixed at room temperature with 4% paraformaldehyde and 15% sucrose for 30 min and maintained in PBS buffer to estimate the total F-actin content. After that, slices were cut into 25 µm sections using a cryostat (Leica CM1900) and incubated with 1 µM of the F-actin-binding toxin phalloidin (Acti-Stain 488 Phalloidin PHDG1, Cytoskeleton Inc., CO, USA) for 1 h. Additionally, hippocampal sections were co-stained with DAPI (Sigma Aldrich; 1:1000) to label nuclei. Digital images were acquired in an upright confocal Eclipse Nikon 80i microscope (Nikon Instruments, NY, USA) equipped with a 20X objective. The fluorescence intensity was measured using the Image J software

(version 1.49v; NIH, MD, USA). All the image preparations were performed by THE Photoshop software (Adobe, CA, USA).

F-actin/G-actin assay

The relative amounts of filamentous (F-actin) and monomeric actin (G-actin) were quantified as previously described [53]. Briefly, hippocampal slices previously stabilized for 1 h with oxygenated ACSF were lysed and homogenized in the presence of conditions that stabilize F-actin and G-actin using an F/G actin commercial assay (F/G actin *in vivo* assay BK037, Cytoskeleton Inc., CO, USA). Then, the homogenates extracts were ultracentrifuged at 100,000 g for 1 h at 37 °C to separate F-actin (pellet) and G-actin (supernatant) fractions. F-actin pellet was resuspended in a depolymerizing buffer (BK037, Cytoskeleton Inc., CO, USA) and then F- and G-actin fractions were diluted in loading buffer (50 mM Tris-HCl, 2% SDS, 10% glycerol, 1% beta-mercaptoethanol and bromophenol blue). Samples were resolved on 12% SDS-PAGE and detected via Western blot analysis using specific antibodies against all the actin isoforms (rabbit anti-actin, BK037 Cytoskeleton Inc.; 1:500) and visualized by ECL (Pierce, Thermo Scientific, IL, USA). The F/G-actin ratio in hippocampal slices was calculated according to the density using the Image J software (version 1.49v; NIH, MD, USA).

Statistics

All data were presented as mean \pm standard error of the mean (SEM). All statistical analyses were performed using GraphPad Prism 9 software (GraphPad Software Inc., CA, USA). For neuron morphology and spine and synapse data, values for single cells were averaged for each animal and then per genotype. For the mean apical and basal dendritic length, and all spine and synapse data, a two-tailed Student's t-test was performed.

Results

PANX1 ablation increases neural excitability without affecting the spontaneous Glutamate release

We determined the impact of the PANX1 deletion on the excitatory synaptic strength upon basal conditions, by using whole-cell current- and voltage-clamp recordings in CA1 hippocampal neurons from PANX1-KO mice and WT littermates (Fig. 1). First, we examined the impact of PANX1 ablation on the intrinsic electrical properties of hippocampal pyramidal neurons (Table 1). We observed that PANX1-KO neurons displayed a lower threshold for action potential discharge (Fig. 1, A and B; WT versus KO * $p=0.0430$, Man-Whitney test). These changes in excitability seem to not be mediated by changes in the intrinsic passive properties of CA1 hippocampal neurons as WT and PANX1-KO neurons exhibited similar resting membrane potential, input resistance, and whole-cell capacitance (Table 1). Since passive properties were unchanged, we explored for modifications in voltage-gated ionic currents (Fig. 1, C and D). No apparent differences in I-V curves were observed (Fig. 1D), although we cannot rule out that selective ionic currents could be different between groups.

Next, we evaluated whether the variations in excitability in PANX1-KO neurons affect the synaptic transmission. We analyzed evoked basal synaptic transmission mediated by AMPAR and NMDAR by generating input-output curves measured as extracellular field excitatory postsynaptic potentials (FP) at different stimulus intensity (Fig. 1E to L). The slope and the fiber volley (FV) amplitudes of AMPAR- and NMDAR-mediated FPs (AR- and NR-FP) were similar between WT and PANX1-KO conditions, suggesting no changes in basal synaptic transmission. However, it is noteworthy that evoked AR- and NR-FP from PANX1-KO neurons exhibited an increased tendency to show population spikes at growing intensities (Fig. 1, H and L), revealing latent greater excitability of the PANX1-KO neurons. To further evaluate these differences, we examined the effect of PANX1 ablation on the release probability (P_r), by estimating two principal forms of short-term synaptic plasticity: paired-pulse ratio (PPR) and use-dependent depression. The PPR was measured as the relative strength of the second of two consecutive synaptic events, which is inversely related to P_r [54]. The use-dependent depression of the synaptic strength was measured as the response to a high-frequency stimulus train [46,55]. Analysis of the PPR revealed no changes between experimental groups, suggesting no alteration in the P_r evaluated by this mean ($p=0.1336$; Fig. 2, A and B). In addition to modifications in the release-probability, changes in neurotransmitter release can result from alterations in the size of the ready-releasable pool (RRP) of synaptic vesicles. Thus, we evaluated the used-dependent depression during a 14 Hz stimulus train, which is an estimation of the size of the RRP [56]. We observed a remarkable difference in the EPSCs evoked by the train of 14 Hz [45,57] (Fig. 2, C to E). After the initial increase in the EPSC amplitude, in WT animals, we observed a progressive depression, consistent with a gradual depletion of the RRP recruited by the train (Fig. 2C). Interestingly, we obtained persistent facilitation throughout the whole stimulatory train in PANX1-KO neurons, which was reflected in the normalized curve of EPSCs (WT versus KO $**p=0.0017$, 2way ANOVA test; Fig. 2D) and the cumulative current amplitude that were significantly different between experimental groups (WT versus KO $***p=0.0002$, 2way ANOVA test; Fig. 2E). Taken together these results suggest that most of the decrease in the EPSC amplitudes cannot be accounted by a change in the P_r but could be due to a decrease in the RRP.

Excitatory short-term synaptic plasticity, particularly synaptic depression may also depend on postsynaptic mechanisms such as desensitization or saturation of AMPARs and/or NMDARs [58]. Hence, we tested for the contribution of postsynaptic receptors in the increased facilitation observed in PANX1-KO CA1 neurons by estimating an NMDAR- to AMPAR-mediated EPSCs ratio (NR/AR) and a PPR for AR- and NR-mediated EPSCs respectively (Fig. 2, F to I). We found that NR/AR was indistinguishable between groups, although NR- and AR-mediated currents were reduced in PANX1-KO mice compared to WT littermates (Fig. 2, F and G). Similarly, we observed that the PPR elicited by NR- and AR-mediated EPSC were comparable between groups (Fig. 2, H and I).

Next, we analyzed the impact of the PANX1 ablation on the spontaneous synaptic activity, by recording spontaneous and miniature excitatory postsynaptic currents (sEPSCs and mEPSCs). We observed that either the frequency or the amplitude of sEPSCs were similar between groups, indicating PANX1 ablation does not affect the basal glutamate release (Fig. 3, A to D). However, we found that the absence of

PANX1 increases the amplitude of mEPSCs (Fig. 3, E to H). PANX1-KO neurons exhibit a higher amplitude of mEPSCs compared to WT (WT versus KO * $p=0.0104$, Man-Whitney test), but the frequency of mEPSCs was unaltered between groups. We also estimated a multiplicity index, an approximation to estimate the number of releasing sites and functional synaptic contacts [49,48] (see methods; Fig. 2, G and H). Interestingly, we found that the multiplicity index in PANX1-KO CA1 neurons was significantly lower than that observed in WT neurons (WT versus KO * $p=0.0012$, Man-Whitney test; Fig. 2 H), suggesting that in the PANX1-KO neurons could establish less functional contacts or possess fewer releasing sites.

Taken together, these results indicate that spontaneous neurotransmission is unaltered in PANX1-KO CA1 neurons, but evoked glutamate release seems prompt to respond to activity demand. Furthermore, PANX1 ablation enhances neural excitability and suggests that PANX1-KO neurons could hold homeostatic-like mechanisms to maintain synaptic transmission.

Increased dendritic arborization and dendritic spine maturity of hippocampal CA1 pyramidal neurons from PANX1-KO mice

As PANX1 ablation might induce adjustments in the network-connectivity and neuron excitability, we analyzed the impact of PANX1 ablation on the morphology of Golgi-stained neurons at dendrite and dendritic spine levels (Fig. 4). A significantly higher dendritic branching and dendritic length were observed in CA1 hippocampal neurons from PANX1-KO mice compared to age-matched WT animals (Fig. 4, A to E). In addition, PANX1-KO neurons exhibited longer dendrites (Fig. 4B) with almost twice branch points (Fig. 4C) in both apical and basal dendrites (Fig. 4D), showing a great number of dendrites throughout the proximal to distal distance from the soma in *Stratum radiatum* layer (Fig. 4E). Furthermore, Sholl's analysis also revealed that PANX1-KO neurons displayed a significantly increased branch order indicative of a greater dendritic complexity in the apical and basal compartments of the CA1 region (Fig. 4, F and G). Concomitantly, analysis of dendritic segments of Golgi-impregnated neurons (Fig. 4H) revealed similar dendritic spines density (Fig. 4I), but a significantly increased dendritic spine length (Fig. 4J) in basal dendrites between WT and PANX1-KO mice. Interestingly, we classified dendritic spines based on their morphology in mature (mushroom- and cup-shaped) and immature spines (filopodia, thin and stubby). We observed that, in general, KO neurons exhibited a greater proportion of mature spines than WT neurons (Fig. 4, K to L), indicating that the absence of PANX1 also induces significant structural changes in spine morphology. Together these data suggest that the lack of PANX1 promotes a significant modification in neuronal morphology.

Structural and molecular remodeling of synapses in hippocampal CA1 pyramidal neurons from PANX1-KO animals

Next, we examined the effect of PANX1 ablation on the synaptic structure by electron microscopy (Fig. 5). We found that CA1 hippocampal neurons from KO mice frequently exhibited compound synapses, either multi-innervated spines or an axon terminal contacting multiple spines (Fig. 5, A and B; Table 2; fig. S1). Furthermore, analysis of compound synapses revealed an increase in the proportion of multiple synaptic contacts in PANX1-KO mice compared to WT animals (Fig. 5, A and B; Table 2; fig. S1). Moreover, KO CA1

neurons displayed more synaptic contacts throughout the apical dendritic tree (Fig. 5C). Also, we found longer PSD size in KO neurons (Fig. 5D). Remarkably, the number of small clear vesicles was significantly higher in KO spines compared to WT (Fig. 5, E and F), in both, the total vesicle docked to the axon terminal membrane as well as the docked vesicles at the active zone (Fig. 5, G to H).

We next tested whether the PANX1 ablation causes a major effect on the synaptic protein content. Early studies have shown that PANX1 is expressed by neurons and glia [59] and accumulates preferentially in the PSD of cortical and hippocampal neurons, colocalizing with postsynaptic proteins such as AMPAR and PSD-95 [60]. Accordingly, we verified these observations by isolating hippocampal synaptoneuroosomes and subsequent separation into PSD-enriched fractions and synaptic membranes devoid of PSD (SM) (Fig. 5I). Interestingly, we detected the presence of PANX1 in both SM- and PSD-enriched fractions suggesting that Panx1 is expressed in pre-and post-synaptic terminals. Although no apparent changes in the overall protein patterns were revealed by the Coomassie blue-stained gel electrophoresis (fig. S2A), western blot from whole hippocampal tissue showed modifications in several synaptic proteins (fig. S2, C and D). In this regard, we found a significant increase in presynaptic proteins such as synaptophysin (SYP) and postsynaptic proteins including, PSD-95 and SAP-102, in both whole hippocampal tissue (fig. S2, C and D) and synaptic enriched fractions (Fig. 5I). Overall, these results suggest that PANX1 lacking produces a major restructuring of the pre-and post-synaptic composition, consistent with the increase in synaptic connectivity.

Lack of PANX1 promotes F-actin formation in hippocampal neurons via the activation of Rac1 and depression of the RhoA small-GTPases.

As the actin cytoskeleton dynamically regulates the morphology of dendrites and spines, the trafficking of glutamate receptors, and the molecular organization of PSD [61], we explored whether the morphological changes observed in PANX1-KO neurons were related to actin cytoskeletal remodeling. Actin exists in a dynamic equilibrium between F-actin and G-actin forms, which are abundant in both pre-and post-synaptic compartments [61]. Therefore, we isolated actin filaments and monomers from hippocampal slices to estimate an F-actin/G-actin ratio (F/G) as an estimation of actin polymerization. We found that the F/G ratio was significantly higher in PANX1-KO compared to WT slices (Fig. 6A), suggesting that PANX1 ablation favors actin polymerization. Additionally, we investigated the impact of the PANX1 ablation on the F-actin content in brain slices of WT and PANX1-KO mice, by visualization of the phalloidin fluorescence, a toxin that specifically binds to F-actin [62]. We observed a higher phalloidin reactivity in the brain slices from PANX1-KO compared to WT mice (Fig. 6B), suggesting that PANX1 ablation promotes the F-actin assembly. We reasoned that if PANX1 ablation promotes the formation of F-actin, then regulatory proteins that control actin dynamics and organization could mediate this effect. Thus, we evaluated the levels of actin-binding proteins (ABPs) and the expression of the Rho-small-GTPase family, which are master regulators of the actin cytoskeleton [63]. Western blot analysis revealed an increased expression of Arp3, Drebrin, Cortactin 1, Rac1, Cdc42, and RhoA in hippocampal homogenates from PANX1-KO compared to WT samples (Fig. 6, D and E), indicating that the PANX1 deficiency affects actin remodeling by altering the expression of ABPs and small Rho GTPases. Rho

GTPases are important molecular “switches” that transduce extracellular signals to the actin cytoskeleton [63,61]. RhoA, Rac1, and Cdc42 are members of the Rho GTPases family, implicated in the maintenance and reorganization of dendritic structures [64,65]. Since the Rho GTPase family regulates actin dynamics, we hypothesize that PANX1 channels may control the expression and activity of the Rho GTPases. We observed significantly increased levels of the active forms of Rac1 in PANX1-KO mice compared to the WT samples and, unexpectedly, we also found a dramatic reduction in the activated form of RhoA in PANX1-KO tissues (Fig, 6 F and G). On the contrary, there were no significant differences in the expression of the activated form of Cdc42.

All these data support a modulatory role of PANX1 which seems to be dependent on the actin cytoskeleton remodeling for basal formation and activity of synapses.

Discussion

PANX1 channels are non-selective channels essential for cellular communication under physiological and pathological conditions [4,66]. At the CNS, they have been proposed to act as negative modulators of neuronal activity as PANX1 deletion, its knockdown as well as its pharmacological inhibition enhances glutamatergic neurotransmission, LTP, and neurite outgrowth [30,31,33,67]. Moreover, overexpression of PANX1 has been associated with neuronal hyperactivity and death, and aberrant PANX1 activity has been observed in several brain disorders, including ischemia [24,25], epilepsy [26,27] and Alzheimer’s disease [29]. Therefore, the expression and activity of PANX1 channels appear to be critical for the proper functioning of brain circuits and especially relevant in the onset of synaptic disorders. This work explored the consequences of the long-term ablation of PANX1 in CA1 excitatory synaptic structure and function, actin dynamic and in pyramidal neuron morphology. By using electrophysiological, biochemical, and structural approaches we demonstrated that in the absence of PANX1 compensatory mechanisms operate, producing alterations in Rho-GTPases and remodeling of the actin cytoskeleton. Modifications in the actin dynamics enhanced the dendritic branching and spine maturity in hippocampal neurons leading to modifications in the number of synaptic contacts in the brain of PANX1-KO mice compared to their WT littermates.

The ablation of PANX1 perturbs neuronal excitability without affecting the spontaneous release of glutamate.

Under intense neuronal activity, such as during the stimulation to evoke input/output curves, either the absence or the blockade of PANX1 induces an increase in the excitatory synaptic transmission [30,31,67]. However, it is still unknown how PANX1 could affect synaptic transmission under basal conditions. Therefore, we monitored glutamatergic neurotransmission and synaptic connectivity to determine whether the absence of PANX1 elicits adaptations to regulate synaptic strength. We found that CA1 pyramidal neurons from PANX1-KO mice exhibited a lower threshold for action potential and fired more action potentials in response to a depolarizing current ramp (Fig 1). Nevertheless, we found that PANX1 ablation does not affect the intrinsic membrane properties of CA1 neurons, nor does it affect the I-V

relationship, although we cannot rule out that selective ionic currents might be affected. In this regard, similar changes in the threshold for AP discharges have been associated with neuronal maturation and homeostatic mechanisms [68,69]. Furthermore, similar homeostatic modifications have been produced by changes in the activity of different ion channels in CA1 neurons [70] including potassium current I_D [71], hyperpolarization-activated current I_h [72] and persistent TTX-sensitive sodium current (I_{NAP}) [73]. Interestingly, changes in the KCC2 transporter, which regulates neuronal chloride gradients and GABA signaling, also modulates intrinsic neuronal excitability [74], suggesting that GABA transmission could be an important factor affected in PANX1-KO neurons. Thus, although inhibitory transmission was not addressed in the present study, modifications in the excitatory/inhibitory (E/I) balance is an aspect that deserves to be considered and require further investigation.

In addition to a large pore conformation with high conductance (100-550 pS) that mediates a non-selective ionic flux and ATP release [16,6,14], PANX1 channels also show a constitutive small pore activity characterized by low conductance (50-80 pS) driving a chloride permeability at negative voltages and outwardly rectifying current-voltage relations [7-10], which could influence the electrical properties of the cells and that can to explain the modifications in the action potential threshold upon PANX1 ablation. Accordingly, a recent report revealed a higher excitability in the hippocampus of PANX1-KO mice [75].

To test if excitability changes involved modifications in glutamatergic synaptic transmission, we employed electrophysiological recording of evoked (fEPSCs) and spontaneous (sEPSCs, and mEPSPs) synaptic events. We did not find significant differences either in the initial slope of fEPSPs or afferent FV amplitude, suggesting non-apparent changes in the efficacy of evoked excitatory synaptic transmission between PANX1-KO and WT neurons. However, AR-and NR-FP revealed that PANX1-KO neurons exhibit an enhanced tendency to fire pop-spikes consistent with an impairment in the E/I balance or a modification in the intrinsic excitability of the CA1 neurons. Since GABAergic neurons regulate the activity of principal neurons and modulate the oscillatory activity of neural networks, the inhibitory GABAergic transmission and oscillatory activity upon PANX1 intervention needs to be evaluated in future.

The latent higher excitability revealed by the changes in the firing threshold and the generation of pop-spikes seem not due to an increase in the spontaneous basal synaptic transmission as the frequency and the amplitude of the sEPSCs were indistinguishable between groups. Likewise, the frequency of mEPSCs were similar, indicating that spontaneous synaptic activity is normal in PANX1-KO neurons (Fig. 1, D to F). However, the amplitude of mEPSCs was higher which could correlate with the higher excitability showed by these neurons. The fact that spontaneous neurotransmission was unaltered but evoked glutamate release seems prompted to respond to activity demand, suggesting that PANX1-KO CA1 neurons likely utilizing different molecular machinery, segregated at distinct postsynaptic sites as has been previously reported [76]. These spontaneous events independent of action potentials inform about the potential locus for synaptic modification. The amplitude of mEPSCs is thought to reflect changes in the expression (number) or activity (conductance) of ionotropic glutamate receptors; meanwhile, changes in the frequency of mEPSCs has been related to presynaptic mechanisms such as the P_r and/or the number of

synapses [77]. The fact that the amplitude of mEPSCs was higher in PANX1-KO neurons strongly supports postsynaptic modifications, although we cannot discard that the lack of PANX1 also affects pre-synaptic transmission mechanisms, as we will discuss later.

Our observations differ from those reported upon PANX1 blockade or interfering with the NMDAR-PANX1-Src kinase pathway inducing an increase in the sEPSC frequency [67]. Although Bialecki et al. described similar results in conditional PANX1-KO neurons, those effects were seen in younger animals. Thus, when we evaluated synaptic responses in our conditions, we believed that long-term homeostatic mechanisms could occur, which permit to maintain the synaptic transmission in the adult hippocampus, without alterations in the spontaneous neurotransmitter release. Nevertheless, we cannot discard the contribution of presynaptic TRPV1-mediated facilitation of glutamate release upon PANX1-ablation observed by the authors in our experimental conditions [67].

The readily releasable pool of synaptic vesicles is increased in PANX1-KO neurons.

In the adult PANX1-KO hippocampus, we previously reported an increased induction of LTP and a lower capacity to induce LTD, which was even a potentiation instead a depression using standard electrophysiological protocols [30,31]. Despite that, the chemical induction of LTD revealed that PANX1-KO synapses have all the protein machinery to support this plastic modulation [30,31]. Our present findings show that in response to a use-dependent depression during a high-frequency stimulus train, PANX1-KO neurons exhibit a sustained response indicating a greater size of RRP (Fig 2). This observation could explain the potentiated response observed in PANX1-KO slices after the applying of a protocol that induces LTD in WT animals [30,51].

An increase in the glutamate release could result from increasing the number of Ca^{2+} -responsive vesicles (i.e., an increase in the RRP), or an increase in the P_r . The examination of the PPR revealed no change between groups. However, the use-dependent depression induced by a 14 Hz stimulus train showed a reluctance of the PANX1-KO synapses to deplete the RRP vesicles evoked by the high frequency stimulation. Consistently, cumulative EPSCs were significantly increased at PANX1-KO synapses, suggesting that the pool of synaptic vesicles immediately available for release could be greater in PANX1-KO neurons.

Interestingly, recent evidence highlights the role of PANX1 channels in the homeostatic adjustment of synaptic strength in hippocampal cultures upon chronic inactivity [43]. Using the immunodetection of the glutamate-transporter 1 (vGlut1) as an index of the presynaptic strength, Rafael et al., reported that PANX1 channels are required for the compensatory vGlut1 upregulation in presynaptic terminals and the adjustment of synapse density under chronic inactivity.

Long-term PANX1 ablation affects structural connectivity

The present study also showed that the multiplicity index, an estimation of the number of releasing sites or likely synaptic contacts [48,49], was significantly lower in PANX1-KO neurons (Fig 3J). This is in

contrast with the ultrastructural findings that revealed a greater number of synaptic contacts in PANX1-KO neurons (Fig 5). In this regard, the highly branched dendritic tree of central neurons defines how neurons can receive synaptic inputs from other neurons and strongly influences how these inputs are integrated to allow the signal transmission and computation [78]. Our results showed a more complex morphology of CA1 neurons from PANX1-KO brains as revealed by the intersection profiles obtained by counting the number of dendritic branches at a given distance from the soma. PANX1-KO neurons displayed longer dendrites with more ramifications in both apical and basal segments and higher branch order. Indeed, this greater dendritic complexity supposed that PANX1-KO CA1 neurons could possess the morphology, structure, and protein composition for more increased connectivity. Indeed, PANX1-KO neurons exhibit a more significant percentage of mature-like dendritic spines, a higher proportion of multiple synaptic contacts, spines with a larger PSD size, and a higher number of synaptic vesicles per bouton or active zone compared to WT neurons (Fig 5D-F). Accordingly, the results obtained under depletion experiments indicate that PANX1-KO mice exhibit a greater size of the RRP as evidenced by the increase in the synaptic responses after the subsequent stimuli. In this regard, similar relationships between the number of vesicles in the docked vesicle-pool, the size of the RRP, the active zone and the PSD sizes in hippocampal synapses have been previously reported [79]. Moreover, PSD- and SM-enriched fractions obtained from hippocampal tissue disclosed an enhanced expression of pre- and post-synaptic proteins (Fig 5H) suggesting that PANX1 ablation might induce compensatory modifications in both compartments. These data demonstrated that morphological changes in dendritic arborization and spines, along with a change in the synaptic protein composition, likely reflect a modification in the remodeling of the neuronal cytoskeleton. We tested this hypothesis by evaluating the organization of the actin cytoskeleton. Actin cytoskeleton transits in a dynamic equilibrium between F-actin and G-actin forms, abundant in presynaptic terminals and postsynaptic dendritic spines [61]. Furthermore, this equilibrium between G-actin and F-actin is finely and rapidly regulated during activity by many postsynaptic ABPs. In this study, we reported that PANX1-KO neurons exhibit higher content of F-actin, suggesting that PANX1 ablation promotes a disequilibrium in actin dynamics towards polymerization. In support of a potential regulatory role of PANX1 over the actin cytoskeleton, it has been previously reported that PANX1 directly binds to F-actin [80] and the actin-related protein Arp3 [33], which is the main component of the Arp2/3 complex involved in *de novo* nucleation and branching of F-actin [81]. Moreover, PANX1 has been implicated in several cell behaviors reliant on the actin rearrangements. In this regard, down-regulation of the PANX1 activity promotes neurite outgrowth, cell migration [82,33], and dendritic spines development [32], suggesting that PANX1 activity limits neuronal actin cytoskeleton remodeling.

The mammalian Rho family of small GTPases are key regulators that control the organization and dynamics of the actin cytoskeleton [63]. Among them, Rac1, Cdc42, and RhoA play a major role in dendritic spine dynamics, connecting signals from the postsynaptic receptors to changes in ABPs and hence, actin polymerization/depolymerization [64,65]. While Rac1 and Cdc42 activation promote spine formation and stabilization, RhoA activation leads to spine retraction and pruning [64,83,65]. Accordingly, we found that hippocampal tissue from PANX1-KO mice exhibits enhanced Rac1, Cdc42, and RhoA levels

along with selective ABPs including Arp3, Drebrin, and Wave-1. Interestingly, the active form of Rac1, but not Cdc42, was significantly increased in hippocampal homogenates from PANX1-KO mice. In contrast, the active form of RhoA was almost absent, consistent with their antagonistic role in dendritic and spine morphology [83]. At this point, downstream effector of Cdc42 and Rac1, such as N-WASP and Arp3, promote the reorganization of the actin cytoskeleton leading to rapid stabilization of dendritic spines [84], while RhoA effectors such as ROCK and formins mDia1 and mDia3 promote actin depolarization and spine instability [85-87], suggesting that the Rho GTPase signaling could be involved in the morphological effects observed in PANX1-KO mice. In this regard, recently it was described a non-canonical RhoA-mDia-HDAC6 signaling pathway for α 1AR activation of Panx1 channels [88] according with the previously reported reduction in ATP release via PANX1 channels after RhoA inhibition[89]. Thus, it appears that the signaling-cascades mediated by PANX1 channels control the steady-state activity levels of the small Rho GTPases Rac1 and RhoA, but the specific mechanism by which Rac1/RhoA impact on the actin cytoskeleton dynamics upon PANX1 absence remains to be elucidated.

These findings revealed an imbalance in the equilibrium towards spines more mature, driven by an enhanced actin polymerization, implying a more static than plastic synaptic architecture. These observations can also explain the previously reported difficulty to inducing LTD mechanisms which implies a retraction or reduction in the size and number of dendritic spines and a higher depolymerization of actin filaments[30,51]. In fact, despite PANX1 ablation has been associated with enhanced glutamatergic neurotransmission, LTP, and neurite outgrowth [30,31,33], alterations in learning flexibility, such as novel object recognition, spatial memory, and anxious behaviors have been described in PANX1-KO mice [51,31]. Nevertheless, the animals preserve their ability to learn, so compensatory or homeostatic mechanisms must operate to maintain the plasticity of the adult brain at cognitively significant levels. Therefore, PANX1 expression and activity in the brain seems to be critical to the proper functioning of neural circuits.

Overall, the results presented here demonstrated that the long-term ablation of PANX1 channels promotes a sequence of functional and morphological changes in hippocampal CA1 neurons. Interestingly, the present data also gives evidence for a possible link between PANX1 and Rho GTPase-dependent regulation of the actin cytoskeleton. Thus, the functional interaction between PANX1 channels and Rho-GTPases could be of pivotal relevance considering that numerous brain disorders such as neuropsychiatric and neurodegenerative conditions develop with abnormalities in the neuronal actin cytoskeleton.

Declarations

Acknowledgments: We thank to Alejandro Munizaga and Oscar Ardiles for technical assistance in EM experiments. We also thanks to Enzo Seguel and Leticia Toledo for animal care supervision, and Linda Olszewski for proofreading of the manuscript.

Code Availability: Not applicable.

Author contributions: CF-M, FG-R, MA-P, OS, and AOA designed the research; CF-M, FG-R, MA-P, OS, EM, DL-E, AMG-J and AOA performed experiments, analyzed data, and contributed to figures. MF, ADM, and AMG-J, contributed to analytic tools, CF-M, AMG-J, MF, ADM, and AOA wrote the paper.

Funding: This work was supported by FONDECYT N°11150776 and 1201342 (AOA), 11180731 (AMG-J), 1171006 (MF), 1171240 (ADM); Millennium Institute ICM-ANID ICN09-022 (AOA, AMG-J and ADM); ANID Doctorate Fellowship 21190247 (CF-M), 21190642 (FG-R) and 21181214 (OS).

Data and materials availability: All data needed to evaluate the conclusions in the paper are present in the paper or the Supplementary Materials.

Ethics approval. All animals used in this study were maintained in the Animal Facility according to Institutional Animal Care and Use Committee policies of the Universidad de Valparaiso (BEA064-2015 and BEA160-20).

Consent to Participate: Not applicable

Consent for Publication: Not applicable

References

1. Deng Z, He Z, Maksaev G, Bitter RM, Rau M, Fitzpatrick JAJ, Yuan P (2020) Cryo-EM structures of the ATP release channel pannexin 1. *Nat Struct Mol Biol* 27 (4):373-381. doi:10.1038/s41594-020-0401-0
2. Michalski K, Syrjanen JL, Henze E, Kumpf J, Furukawa H, Kawate T (2020) The Cryo-EM structure of pannexin 1 reveals unique motifs for ion selection and inhibition. *Elife* 9. doi:10.7554/eLife.54670
3. Ruan Z, Orozco IJ, Du J, Lu W (2020) Structures of human pannexin 1 reveal ion pathways and mechanism of gating. *Nature* 584 (7822):646-651. doi:10.1038/s41586-020-2357-y
4. Decrock E, De Bock M, Wang N, Bultynck G, Giaume C, Naus CC, Green CR, Leybaert L (2015) Connexin and pannexin signaling pathways, an architectural blueprint for CNS physiology and pathology? *Cell Mol Life Sci* 72 (15):2823-2851. doi:10.1007/s00018-015-1962-7
5. Cheung G, Chever O, Rouach N (2014) Connexons and pannexons: newcomers in neurophysiology. *Front Cell Neurosci* 8:348. doi:10.3389/fncel.2014.00348
6. Wang J, Ambrosi C, Qiu F, Jackson DG, Sosinsky G, Dahl G (2014) The membrane protein Pannexin1 forms two open-channel conformations depending on the mode of activation. *Sci Signal* 7 (335):ra69. doi:10.1126/scisignal.2005431
7. Ma W, Compan V, Zheng W, Martin E, North RA, Verkhratsky A, Surprenant A (2012) Pannexin 1 forms an anion-selective channel. *Pflugers Arch* 463 (4):585-592. doi:10.1007/s00424-012-1077-z

8. Nomura T, Taruno A, Shiraishi M, Nakahari T, Inui T, Sokabe M, Eaton DC, Marunaka Y (2017) Current-direction/amplitude-dependent single channel gating kinetics of mouse pannexin 1 channel: a new concept for gating kinetics. *Sci Rep* 7 (1):10512. doi:10.1038/s41598-017-10921-x
9. Wang J, Dahl G (2018) Pannexin1: a multifunction and multiconductance and/or permeability membrane channel. *Am J Physiol Cell Physiol* 315 (3):C290-C299. doi:10.1152/ajpcell.00302.2017
10. Romanov RA, Bystrova MF, Rogachevskaya OA, Sadovnikov VB, Shestopalov VI, Kolesnikov SS (2012) The ATP permeability of pannexin 1 channels in a heterologous system and in mammalian taste cells is dispensable. *J Cell Sci* 125 (Pt 22):5514-5523. doi:10.1242/jcs.111062
11. Thompson RJ, Jackson MF, Olah ME, Rungta RL, Hines DJ, Beazely MA, MacDonald JF, MacVicar BA (2008) Activation of pannexin-1 hemichannels augments aberrant bursting in the hippocampus. *Science* 322 (5907):1555-1559. doi:10.1126/science.1165209
12. Lopatar J, Dale N, Frenguelli BG (2015) Pannexin-1-mediated ATP release from area CA3 drives mGlu5-dependent neuronal oscillations. *Neuropharmacology* 93:219-228. doi:10.1016/j.neuropharm.2015.01.014
13. Silverman WR, de Rivero Vaccari JP, Locovei S, Qiu F, Carlsson SK, Scemes E, Keane RW, Dahl G (2009) The pannexin 1 channel activates the inflammasome in neurons and astrocytes. *J Biol Chem* 284 (27):18143-18151. doi:10.1074/jbc.M109.004804
14. Bao L, Locovei S, Dahl G (2004) Pannexin membrane channels are mechanosensitive conduits for ATP. *FEBS letters* 572 (1-3):65-68. doi:10.1016/j.febslet.2004.07.009
15. Locovei S, Bao L, Dahl G (2006) Pannexin 1 in erythrocytes: function without a gap. *Proc Natl Acad Sci U S A* 103 (20):7655-7659. doi:10.1073/pnas.0601037103
16. Thompson RJ, Zhou N, MacVicar BA (2006) Ischemia opens neuronal gap junction hemichannels. *Science* 312 (5775):924-927. doi:10.1126/science.1126241
17. Weillinger NL, Lohman AW, Rakai BD, Ma EM, Bialecki J, Maslieieva V, Rilea T, Bandet MV, Ikuta NT, Scott L, Colicos MA, Teskey GC, Winship IR, Thompson RJ (2016) Metabotropic NMDA receptor signaling couples Src family kinases to pannexin-1 during excitotoxicity. *Nat Neurosci* 19 (3):432-442. doi:10.1038/nn.4236
18. Pelegrin P, Surprenant A (2006) Pannexin-1 mediates large pore formation and interleukin-1beta release by the ATP-gated P2X7 receptor. *EMBO J* 25 (21):5071-5082. doi:10.1038/sj.emboj.7601378
19. Billaud M, Lohman AW, Straub AC, Looft-Wilson R, Johnstone SR, Araj CA, Best AK, Chekeni FB, Ravichandran KS, Penuela S, Laird DW, Isakson BE (2011) Pannexin1 regulates alpha1-adrenergic receptor-mediated vasoconstriction. *Circ Res* 109 (1):80-85. doi:10.1161/CIRCRESAHA.110.237594

20. Maldifassi MC, Momboisse F, Guerra MJ, Vielma AH, Maripillan J, Baez-Matus X, Flores-Munoz C, Cadiz B, Schmachtenberg O, Martinez AD, Cardenas AM (2021) The interplay between alpha7 nicotinic acetylcholine receptors, pannexin-1 channels and P2X7 receptors elicit exocytosis in chromaffin cells. *J Neurochem* 157 (6):1789-1808. doi:10.1111/jnc.15186
21. Chekeni FB, Elliott MR, Sandilos JK, Walk SF, Kinchen JM, Lazarowski ER, Armstrong AJ, Penuela S, Laird DW, Salvesen GS, Isakson BE, Bayliss DA, Ravichandran KS (2010) Pannexin 1 channels mediate 'find-me' signal release and membrane permeability during apoptosis. *Nature* 467 (7317):863-867. doi:10.1038/nature09413
22. Narahari AK, Kreutzberger AJ, Gaete PS, Chiu YH, Leonhardt SA, Medina CB, Jin X, Oleniacz PW, Kiessling V, Barrett PQ, Ravichandran KS, Yeager M, Contreras JE, Tamm LK, Bayliss DA (2021) ATP and large signaling metabolites flux through caspase-activated Pannexin 1 channels. *Elife* 10. doi:10.7554/eLife.64787
23. Shestopalov VI, Slepak VZ (2014) Molecular pathways of pannexin1-mediated neurotoxicity. *Front Physiol* 5:23. doi:10.3389/fphys.2014.00023
24. Wei R, Wang J, Xu Y, Yin B, He F, Du Y, Peng G, Luo B (2015) Probenecid protects against cerebral ischemia/reperfusion injury by inhibiting lysosomal and inflammatory damage in rats. *Neuroscience* 301:168-177. doi:10.1016/j.neuroscience.2015.05.070
25. Bargiotas P, Krenz A, Hormuzdi SG, Ridder DA, Herb A, Barakat W, Penuela S, von Engelhardt J, Monyer H, Schwaninger M (2011) Pannexins in ischemia-induced neurodegeneration. *Proc Natl Acad Sci U S A* 108 (51):20772-20777. doi:10.1073/pnas.1018262108
26. Aquilino MS, Whyte-Fagundes P, Zoidl G, Carlen PL (2019) Pannexin-1 channels in epilepsy. *Neurosci Lett* 695:71-75. doi:10.1016/j.neulet.2017.09.004
27. Li S, Zang Z, He J, Chen X, Yu S, Pei Y, Hou Z, An N, Yang H, Zhang C, Liu S (2017) Expression of pannexin 1 and 2 in cortical lesions from intractable epilepsy patients with focal cortical dysplasia. *Oncotarget* 8 (4):6883-6895. doi:10.18632/oncotarget.14317
28. Dossi E, Blauwblomme T, Moulard J, Chever O, Vasile F, Guinard E, Le Bert M, Couillin I, Pallud J, Capelle L, Huberfeld G, Rouach N (2018) Pannexin-1 channels contribute to seizure generation in human epileptic brain tissue and in a mouse model of epilepsy. *Sci Transl Med* 10 (443). doi:10.1126/scitranslmed.aar3796
29. Flores-Munoz C, Gomez B, Mery E, Mujica P, Gajardo I, Cordova C, Lopez-Espindola D, Duran-Aniotz C, Hetz C, Munoz P, Gonzalez-Jamett AM, Ardiles AO (2020) Acute Pannexin 1 Blockade Mitigates Early Synaptic Plasticity Defects in a Mouse Model of Alzheimer's Disease. *Front Cell Neurosci* 14:46. doi:10.3389/fncel.2020.00046

30. Ardiles AO, Flores-Munoz C, Toro-Ayala G, Cardenas AM, Palacios AG, Munoz P, Fuenzalida M, Saez JC, Martinez AD (2014) Pannexin 1 regulates bidirectional hippocampal synaptic plasticity in adult mice. *Front Cell Neurosci* 8:326. doi:10.3389/fncel.2014.00326
31. Prochnow N, Abdulazim A, Kurtenbach S, Wildforster V, Dvorientchikova G, Hanske J, Petrasch-Parwez E, Shestopalov VI, Dermietzel R, Manahan-Vaughan D, Zoidl G (2012) Pannexin1 stabilizes synaptic plasticity and is needed for learning. *PloS one* 7 (12):e51767. doi:10.1371/journal.pone.0051767
32. Sanchez-Arias JC, Liu M, Choi CSW, Ebert SN, Brown CE, Swayne LA (2019) Pannexin 1 regulates network ensembles and dendritic spine development in cortical neurons. *eNeuro*. doi:10.1523/ENEURO.0503-18.2019
33. Wicki-Stordeur LE, Swayne LA (2013) Panx1 regulates neural stem and progenitor cell behaviours associated with cytoskeletal dynamics and interacts with multiple cytoskeletal elements. *Cell Commun Signal* 11:62. doi:10.1186/1478-811X-11-62
34. Bailey CH, Kandel ER (1993) Structural changes accompanying memory storage. *Annu Rev Physiol* 55:397-426. doi:10.1146/annurev.ph.55.030193.002145
35. Ardiles AO, Grabrucker AM, Scholl FG, Rudenko G, Borsello T (2017) Molecular and Cellular Mechanisms of Synaptopathies. *Neural Plast* 2017:2643943. doi:10.1155/2017/2643943
36. Gipson CD, Olive MF (2017) Structural and functional plasticity of dendritic spines - root or result of behavior? *Genes Brain Behav* 16 (1):101-117. doi:10.1111/gbb.12324
37. Turrigiano G (2012) Homeostatic synaptic plasticity: local and global mechanisms for stabilizing neuronal function. *Cold Spring Harb Perspect Biol* 4 (1):a005736. doi:10.1101/cshperspect.a005736
38. Desai NS (2003) Homeostatic plasticity in the CNS: synaptic and intrinsic forms. *J Physiol Paris* 97 (4-6):391-402. doi:10.1016/j.jphysparis.2004.01.005
39. Lee HK, Kirkwood A (2019) Mechanisms of Homeostatic Synaptic Plasticity in vivo. *Front Cell Neurosci* 13:520. doi:10.3389/fncel.2019.00520
40. Davis GW (2013) Homeostatic signaling and the stabilization of neural function. *Neuron* 80 (3):718-728. doi:10.1016/j.neuron.2013.09.044
41. Zhang W, Linden DJ (2003) The other side of the engram: experience-driven changes in neuronal intrinsic excitability. *Nat Rev Neurosci* 4 (11):885-900. doi:10.1038/nrn1248
42. Pozo K, Goda Y (2010) Unraveling mechanisms of homeostatic synaptic plasticity. *Neuron* 66 (3):337-351. doi:10.1016/j.neuron.2010.04.028

43. Rafael A, Cairus A, Tizzoni M, Abudara V, Vituriera N (2020) Glial ATP and Large Pore Channels Modulate Synaptic Strength in Response to Chronic Inactivity. *Mol Neurobiol* 57 (6):2856-2869. doi:10.1007/s12035-020-01919-0
44. Anselmi F, Hernandez VH, Crispino G, Seydel A, Ortolano S, Roper SD, Kessarar N, Richardson W, Rickheit G, Filippov MA, Monyer H, Mammano F (2008) ATP release through connexin hemichannels and gap junction transfer of second messengers propagate Ca²⁺ signals across the inner ear. *Proc Natl Acad Sci U S A* 105 (48):18770-18775. doi:10.1073/pnas.0800793105
45. Schneggenburger R, Meyer AC, Neher E (1999) Released fraction and total size of a pool of immediately available transmitter quanta at a calyx synapse. *Neuron* 23 (2):399-409. doi:10.1016/s0896-6273(00)80789-8
46. Fioravante D, Regehr WG (2011) Short-term forms of presynaptic plasticity. *Curr Opin Neurobiol* 21 (2):269-274. doi:10.1016/j.conb.2011.02.003
47. Moulder KL, Mennerick S (2005) Reluctant vesicles contribute to the total readily releasable pool in glutamatergic hippocampal neurons. *J Neurosci* 25 (15):3842-3850. doi:10.1523/JNEUROSCI.5231-04.2005
48. Fuenzalida M, Aliaga E, Olivares V, Roncagliolo M, Bonansco C (2009) Developmental increase of asynchronous glutamate release from hippocampal synapses in mutant taiep rat. *Synapse* 63 (6):502-509. doi:10.1002/syn.20622
49. Hsia AY, Malenka RC, Nicoll RA (1998) Development of excitatory circuitry in the hippocampus. *J Neurophysiol* 79 (4):2013-2024. doi:10.1152/jn.1998.79.4.2013
50. Risher WC, Ustunkaya T, Singh Alvarado J, Eroglu C (2014) Rapid Golgi analysis method for efficient and unbiased classification of dendritic spines. *PLoS one* 9 (9):e107591. doi:10.1371/journal.pone.0107591
51. Gajardo I, Salazar CS, Lopez-Espindola D, Estay C, Flores-Munoz C, Elgueta C, Gonzalez-Jamett AM, Martinez AD, Munoz P, Ardiles AO (2018) Lack of Pannexin 1 Alters Synaptic GluN2 Subunit Composition and Spatial Reversal Learning in Mice. *Front Mol Neurosci* 11:114. doi:10.3389/fnmol.2018.00114
52. Ardiles AO, Tapia-Rojas CC, Mandal M, Alexandre F, Kirkwood A, Inestrosa NC, Palacios AG (2012) Postsynaptic dysfunction is associated with spatial and object recognition memory loss in a natural model of Alzheimer's disease. *Proc Natl Acad Sci U S A* 109 (34):13835-13840. doi:10.1073/pnas.1201209109
53. Gonzalez-Jamett AM, Baez-Matus X, Olivares MJ, Hinostroza F, Guerra-Fernandez MJ, Vasquez-Navarrete J, Bui MT, Guicheney P, Romero NB, Bevilacqua JA, Bitoun M, Caviedes P, Cardenas AM (2017)

- Dynamin-2 mutations linked to Centronuclear Myopathy impair actin-dependent trafficking in muscle cells. *Sci Rep* 7 (1):4580. doi:10.1038/s41598-017-04418-w
54. Zucker RS, Regehr WG (2002) Short-term synaptic plasticity. *Annu Rev Physiol* 64:355-405. doi:10.1146/annurev.physiol.64.092501.114547
55. Regehr WG (2012) Short-term presynaptic plasticity. *Cold Spring Harb Perspect Biol* 4 (7):a005702. doi:10.1101/cshperspect.a005702
56. Kaeser PS, Deng L, Chavez AE, Liu X, Castillo PE, Sudhof TC (2009) ELKS2alpha/CAST deletion selectively increases neurotransmitter release at inhibitory synapses. *Neuron* 64 (2):227-239. doi:10.1016/j.neuron.2009.09.019
57. Dobrunz LE (2002) Release probability is regulated by the size of the readily releasable vesicle pool at excitatory synapses in hippocampus. *Int J Dev Neurosci* 20 (3-5):225-236. doi:10.1016/s0736-5748(02)00015-1
58. Schneggenburger R, Sakaba T, Neher E (2002) Vesicle pools and short-term synaptic depression: lessons from a large synapse. *Trends Neurosci* 25 (4):206-212. doi:10.1016/s0166-2236(02)02139-2
59. Huang Y, Grinspan JB, Abrams CK, Scherer SS (2007) Pannexin1 is expressed by neurons and glia but does not form functional gap junctions. *Glia* 55 (1):46-56. doi:10.1002/glia.20435
60. Zoidl G, Petrasch-Parwez E, Ray A, Meier C, Bunse S, Habbes HW, Dahl G, Dermietzel R (2007) Localization of the pannexin1 protein at postsynaptic sites in the cerebral cortex and hippocampus. *Neuroscience* 146 (1):9-16. doi:10.1016/j.neuroscience.2007.01.061
61. Dillon C, Goda Y (2005) The actin cytoskeleton: integrating form and function at the synapse. *Annu Rev Neurosci* 28:25-55. doi:10.1146/annurev.neuro.28.061604.135757
62. Faulstich H, Zobeley S, Rinnerthaler G, Small JV (1988) Fluorescent phallotoxins as probes for filamentous actin. *J Muscle Res Cell Motil* 9 (5):370-383. doi:10.1007/bf01774064
63. Hall A, Nobes CD (2000) Rho GTPases: molecular switches that control the organization and dynamics of the actin cytoskeleton. *Philos Trans R Soc Lond B Biol Sci* 355 (1399):965-970. doi:10.1098/rstb.2000.0632
64. Duman JG, Mulherkar S, Tu YK, J XC, Toliaas KF (2015) Mechanisms for spatiotemporal regulation of Rho-GTPase signaling at synapses. *Neurosci Lett* 601:4-10. doi:10.1016/j.neulet.2015.05.034
65. Toliaas KF, Duman JG, Um K (2011) Control of synapse development and plasticity by Rho GTPase regulatory proteins. *Prog Neurobiol* 94 (2):133-148. doi:10.1016/j.pneurobio.2011.04.011

66. Yeung AK, Patil CS, Jackson MF (2020) Pannexin-1 in the CNS: emerging concepts in health and disease. *J Neurochem*:e15004. doi:10.1111/jnc.15004
67. Bialecki J, Werner A, Weilinger NL, Tucker CM, Vecchiarelli HA, Egana J, Mendizabal-Zubiaga J, Grandes P, Hill MN, Thompson RJ (2020) Suppression of Presynaptic Glutamate Release by Postsynaptic Metabotropic NMDA Receptor Signalling to Pannexin-1. *J Neurosci* 40 (4):729-742. doi:10.1523/JNEUROSCI.0257-19.2019
68. Schmidt-Hieber C, Jonas P, Bischofberger J (2004) Enhanced synaptic plasticity in newly generated granule cells of the adult hippocampus. *Nature* 429 (6988):184-187. doi:10.1038/nature02553
69. Desai NS, Rutherford LC, Turrigiano GG (1999) Plasticity in the intrinsic excitability of cortical pyramidal neurons. *Nat Neurosci* 2 (6):515-520. doi:10.1038/9165
70. Wefelmeyer W, Puhl CJ, Burrone J (2016) Homeostatic Plasticity of Subcellular Neuronal Structures: From Inputs to Outputs. *Trends Neurosci* 39 (10):656-667. doi:10.1016/j.tins.2016.08.004
71. Morgan PJ, Bourboulou R, Filippi C, Koenig-Gambini J, Epsztein J (2019) Kv1.1 contributes to a rapid homeostatic plasticity of intrinsic excitability in CA1 pyramidal neurons in vivo. *Elife* 8. doi:10.7554/eLife.49915
72. Gasselín C, Inglebert Y, Ankri N, Debanne D (2017) Plasticity of intrinsic excitability during LTD is mediated by bidirectional changes in h-channel activity. *Sci Rep* 7 (1):14418. doi:10.1038/s41598-017-14874-z
73. Yamada-Hanff J, Bean BP (2013) Persistent sodium current drives conditional pacemaking in CA1 pyramidal neurons under muscarinic stimulation. *J Neurosci* 33 (38):15011-15021. doi:10.1523/JNEUROSCI.0577-13.2013
74. Goutierre M, Al Awabdh S, Donneger F, Francois E, Gomez-Dominguez D, Irinopoulou T, Menendez de la Prida L, Poncer JC (2019) KCC2 Regulates Neuronal Excitability and Hippocampal Activity via Interaction with Task-3 Channels. *Cell Rep* 28 (1):91-103 e107. doi:10.1016/j.celrep.2019.06.001
75. Sudkamp N, Shchyglo O, Manahan-Vaughan D (2021) Absence of Pannexin 1 Stabilizes Hippocampal Excitability After Intracerebral Treatment With Abeta (1-42) and Prevents LTP Deficits in Middle-Aged Mice. *Front Aging Neurosci* 13:591735. doi:10.3389/fnagi.2021.591735
76. Kavalali ET (2015) The mechanisms and functions of spontaneous neurotransmitter release. *Nat Rev Neurosci* 16 (1):5-16. doi:10.1038/nrn3875
77. Kaeser PS, Regehr WG (2014) Molecular mechanisms for synchronous, asynchronous, and spontaneous neurotransmitter release. *Annu Rev Physiol* 76:333-363. doi:10.1146/annurev-physiol-021113-170338

78. Spruston N (2008) Pyramidal neurons: dendritic structure and synaptic integration. *Nat Rev Neurosci* 9 (3):206-221. doi:10.1038/nrn2286
79. Schikorski T, Stevens CF (1997) Quantitative ultrastructural analysis of hippocampal excitatory synapses. *J Neurosci* 17 (15):5858-5867
80. Bhalla-Gehi R, Penuela S, Churko JM, Shao Q, Laird DW (2010) Pannexin1 and pannexin3 delivery, cell surface dynamics, and cytoskeletal interactions. *J Biol Chem* 285 (12):9147-9160. doi:10.1074/jbc.M109.082008
81. Racz B, Weinberg RJ (2008) Organization of the Arp2/3 complex in hippocampal spines. *J Neurosci* 28 (22):5654-5659. doi:10.1523/JNEUROSCI.0756-08.2008
82. Wicki-Stordeur LE, Dzugalo AD, Swansburg RM, Suits JM, Swayne LA (2012) Pannexin 1 regulates postnatal neural stem and progenitor cell proliferation. *Neural Dev* 7:11. doi:10.1186/1749-8104-7-11
83. Tashiro A, Minden A, Yuste R (2000) Regulation of dendritic spine morphology by the rho family of small GTPases: antagonistic roles of Rac and Rho. *Cereb Cortex* 10 (10):927-938. doi:10.1093/cercor/10.10.927
84. Wegner AM, Nebhan CA, Hu L, Majumdar D, Meier KM, Weaver AM, Webb DJ (2008) N-wasp and the arp2/3 complex are critical regulators of actin in the development of dendritic spines and synapses. *J Biol Chem* 283 (23):15912-15920. doi:10.1074/jbc.M801555200
85. Bobo-Jimenez V, Delgado-Esteban M, Angibaud J, Sanchez-Moran I, de la Fuente A, Yajeya J, Nagerl UV, Castillo J, Bolanos JP, Almeida A (2017) APC/C(Cdh1)-Rock2 pathway controls dendritic integrity and memory. *Proc Natl Acad Sci U S A* 114 (17):4513-4518. doi:10.1073/pnas.1616024114
86. Hotulainen P, Llano O, Smirnov S, Tanhuanpaa K, Faix J, Rivera C, Lappalainen P (2009) Defining mechanisms of actin polymerization and depolymerization during dendritic spine morphogenesis. *J Cell Biol* 185 (2):323-339. doi:10.1083/jcb.200809046
87. Qu X, Yuan FN, Corona C, Pasini S, Pero ME, Gundersen GG, Shelanski ML, Bartolini F (2017) Stabilization of dynamic microtubules by mDia1 drives Tau-dependent Abeta1-42 synaptotoxicity. *J Cell Biol* 216 (10):3161-3178. doi:10.1083/jcb.201701045
88. Chiu YH, Medina CB, Doyle CA, Zhou M, Narahari AK, Sandilos JK, Gonye EC, Gao HY, Guo SY, Parlak M, Lorenz UM, Conrads TP, Desai BN, Ravichandran KS, Bayliss DA (2021) Deacetylation as a receptor-regulated direct activation switch for pannexin channels. *Nat Commun* 12 (1):4482. doi:10.1038/s41467-021-24825-y
89. Seminario-Vidal L, Okada SF, Sesma JI, Kreda SM, van Heusden CA, Zhu Y, Jones LC, O'Neal WK, Penuela S, Laird DW, Boucher RC, Lazarowski ER (2011) Rho signaling regulates pannexin 1-mediated ATP release from airway epithelia. *J Biol Chem* 286 (30):26277-26286. doi:10.1074/jbc.M111.260562

Tables

Table 1 Intrinsic passive properties of hippocampal neurons

	WT	PANX1-KO	Mann Whitney test
	(<i>n</i> = 6)	(<i>n</i> = 8)	<i>p</i> -value
V_m (mV)	-64.78±0.51	-68.11±1.42	0.1893
R_{in} (MW)	149.05±3.40	170.15±16.90	0.3357
C_m (pF)	63.50±7.00	77.09±9.16	0.2810
t	9.61±0.80	12.92±1.65	0.0721
Number of AP	9.67±1.72	10±0.92	0.6034
Firing frequency _{200pA}	11.5±4.97	12.65±0.96	0.7802
Firing frequency _{250pA}	13.83±4.66	14±1.82	0.6420
Firing frequency _{300pA}	15.4±5.12	14.5±2.63	0.9130

Input resistance (R_{in}) and resting membrane potential (V_m) were measured in the current clamp on the same cells used to construct I–V curves and determine threshold values. Whole-cell capacitance (C_m) was measured in voltage-clamp on cells used to measure ionic currents. No differences were significant.

Table 2 Morphological classification of synapses

	Compound synapses ¹			Type of compound synapses ²			
	Simple	Double	Triple	I	II	III	IV
WT	80.9±23.3	9.8±1.5	0.80±0.2	2.5±0.6	1.8±0.2	1.5±0.3	0.0±0.0
PANX1-KO	208.0±17.6	58.2±3.3	4.4±0.9	4.0±0.4	15±1.6	6.8±0.8	2.3±0.5

Data are mean ± SEM. *Statistical significance determined by ANOVA ($p < 0.05$) compared to WT group.

¹Number of synapses. Compound synapses refers to double and triple synapses. ²Type I = presynaptic terminal with one spine; Type II= presynaptic terminal with two contacts on the same spine; Type III= presynaptic terminal with two spines; Type IV= presynaptic terminal with three or more contacts.

Figures

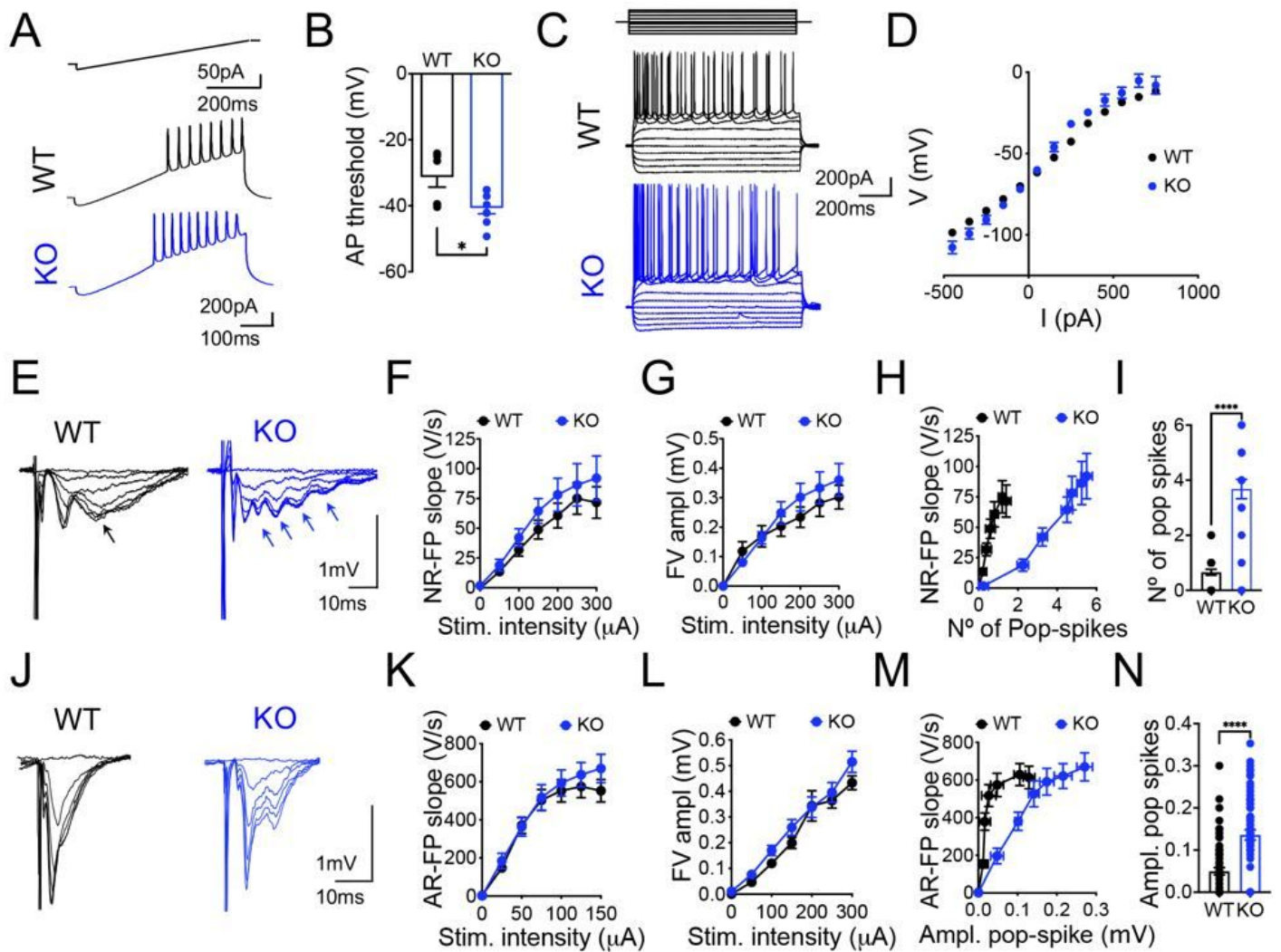


Figure 1

Enhanced excitability but normal glutamatergic synaptic transmission in hippocampal CA1 neurons from PANX1-KO mice. (A) Representative traces of action potential recordings evoked by a current ramp in CA1 neurons of wild-type (WT, black) and PANX1-knockout (KO, blue) mice. (B) Action potential threshold. (C) Representative traces of membrane potential changes in response to the current steps. (D) Current-voltage curves. $n = 7$ (WT) and $n = 8$ (KO) slices from 4 animals, $*p=0.0430$ Mann-Whitney test. (E) Representative traces of input-output curves of pharmacological isolated NMDAR fEPSP (NR-FP) and analysis of the slope (F), fiber volley (FV) amplitude (G), plots of NR-FP slope versus the number of pop spikes (H) and averaged number (N°) of pop spikes (I). $n = 10$ (WT) and $n = 7$ (KO) slices from 3-5 animals, $****p<0.0001$ Mann-Whitney test. (J) Representative traces of input-output curves of AMPAR fEPSP (AR-FP) and analysis of the slope (K), FV amplitude (L), plots of AR-FP slope versus the amplitude of the pop spike (M) and averaged amplitude of pop spikes (N). $n = 22$ (WT) and $n = 25$ (KO) slices from 5-6 animals, $****p<0.0001$ Mann-Whitney test.

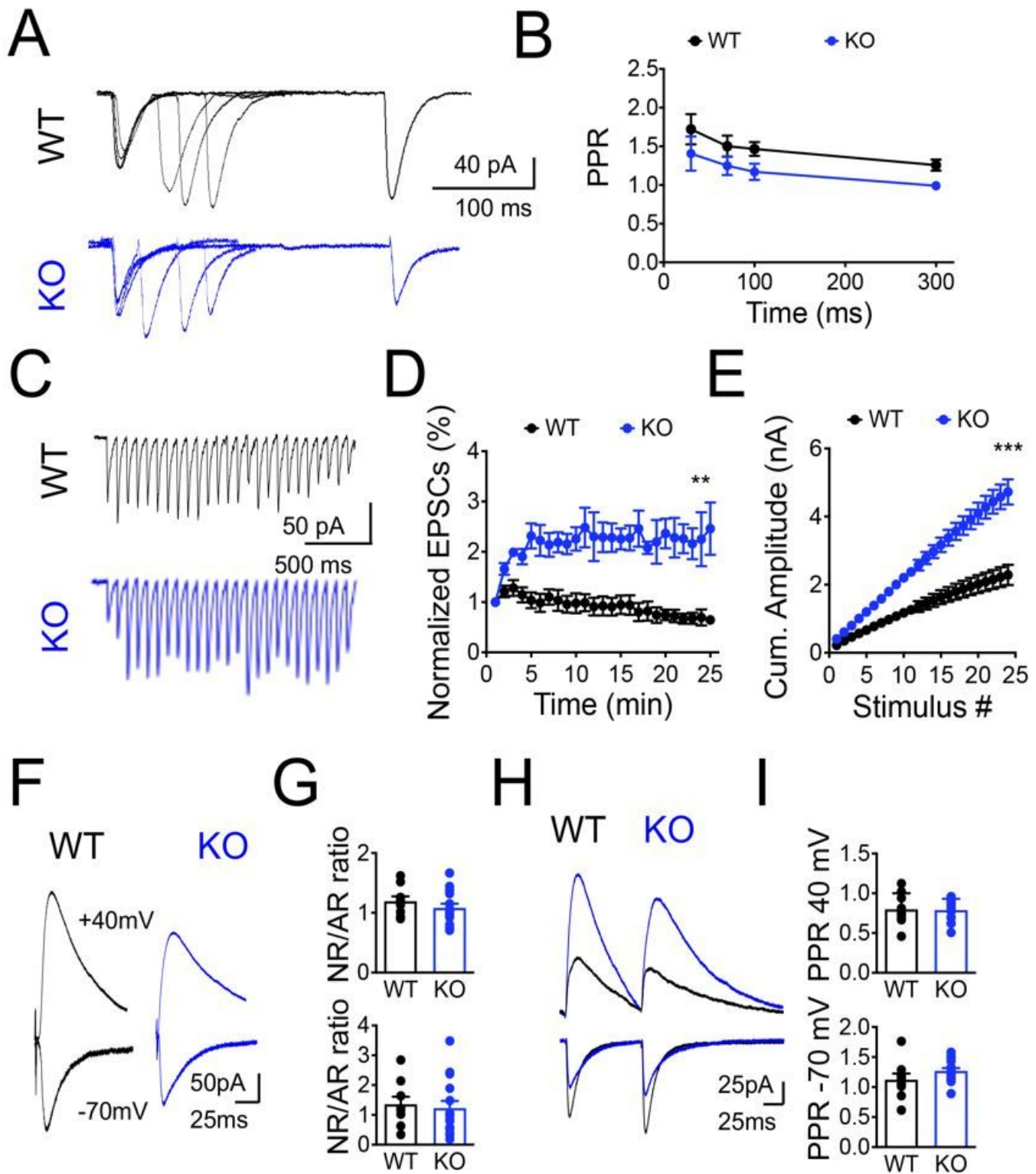


Figure 2

Readily-releasable pool (RRP) and vesicle release probability are increased in PANX1-KO synapses. (A) Representative traces of superimposed paired-pulse responses at variable inter-pulse intervals from wild-type (WT, black) and PANX1-knockout (KO, blue) CA1 neurons. (B) Analysis of paired-pulse facilitation ratio. (C) Representative traces of EPSCs evoked by a train of 25 pulses at 14Hz. (D) Normalized values of EPSCs. $n = 5$ (WT) and $n = 7$ (KO) slices from 3-5 animals, $**p=0.0017$ 2way ANOVA test. (E) Plot of

the cumulative EPSCs versus number of stimuli. $n = 5$ (WT) and $n = 7$ (KO) slices from 3-5 animals, $**p=0.0002$ 2way ANOVA test. (F) Representative traces of NMDAR and AMPAR currents. (F) Analysis of AMPAR to NMDAR (AR/NR) ratio (H) recorded at 40 mV (top) and -70 mV (bottom). (I) Representative traces of AMPAR and NMDAR currents induced by a paired pulse (at 50-ms intervals). (J) Analysis of paired-pulse ratio (PPR) recorded at 40 mV (top) and -70 mV (bottom).

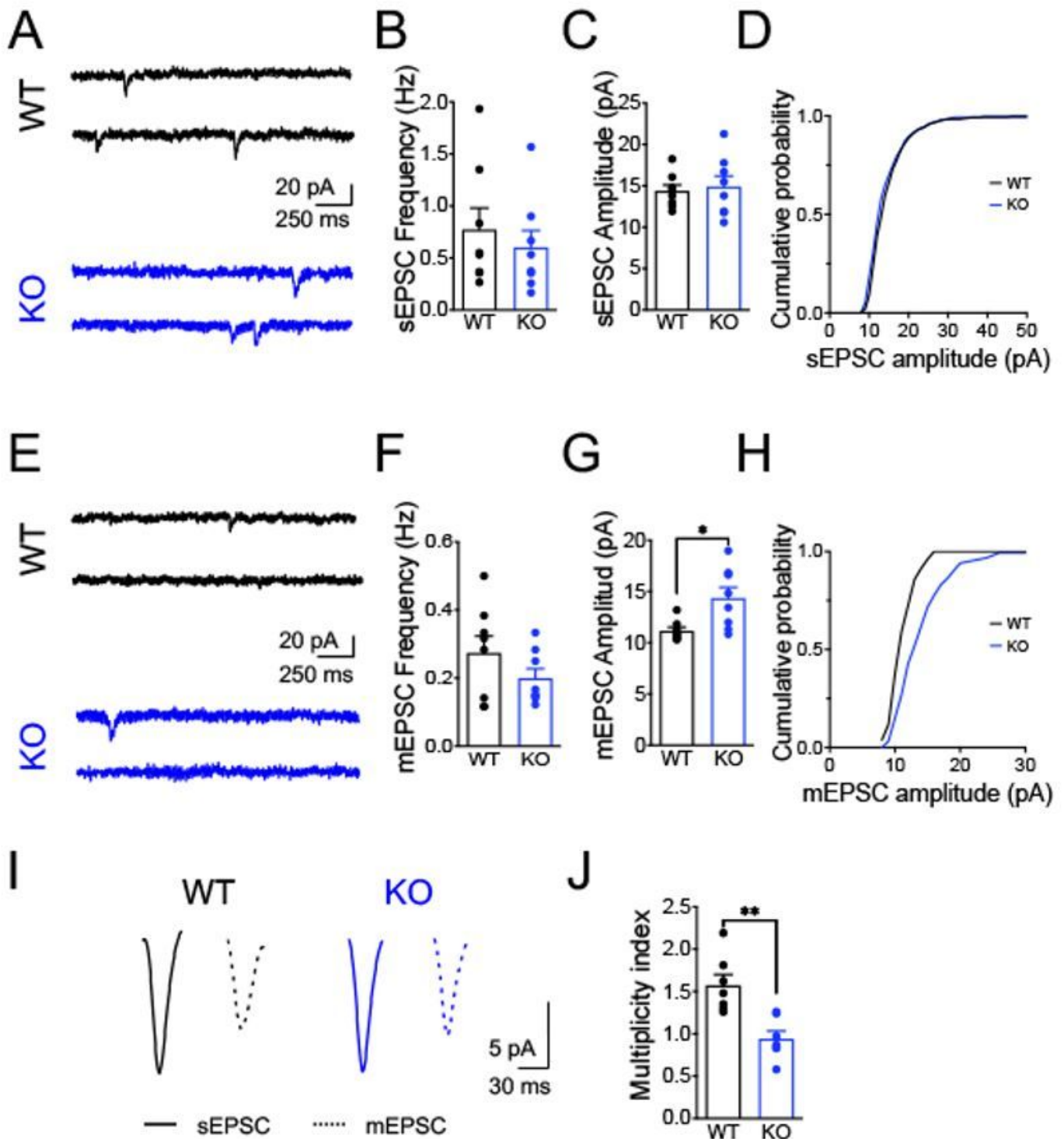


Figure 3

Increased mEPSC amplitude but normal spontaneous release and reduced number of releasing sites in PANX1-KO CA1 neurons. (A) Representative traces of sEPSC events recorded in wild-type (WT, black) and PANX1-knockout (KO, blue) CA1 neurons. (B-C) Analysis of sEPSC frequency (B) and amplitude (C). (D) Cumulative probability plots of the sEPSC amplitude distribution. (E) Representative traces of mEPSC events (F-H) Analysis of mEPSC frequency (F) and amplitude (G). n = 8 (WT) and n = 8 (KO) slices from 3-5 animals, *p=0.0104 Mann-Whitney test. (H) Cumulative probability plots of the mEPSC amplitude distribution. (I) Averaged traces of individual sEPSC (continuous line) and mEPSC (dotted line) events. (J) Analysis of the multiplicity index. n = 7 (WT) and n = 7 (KO) slices from 3-5 animals, **p=0.0012 Mann-Whitney test.

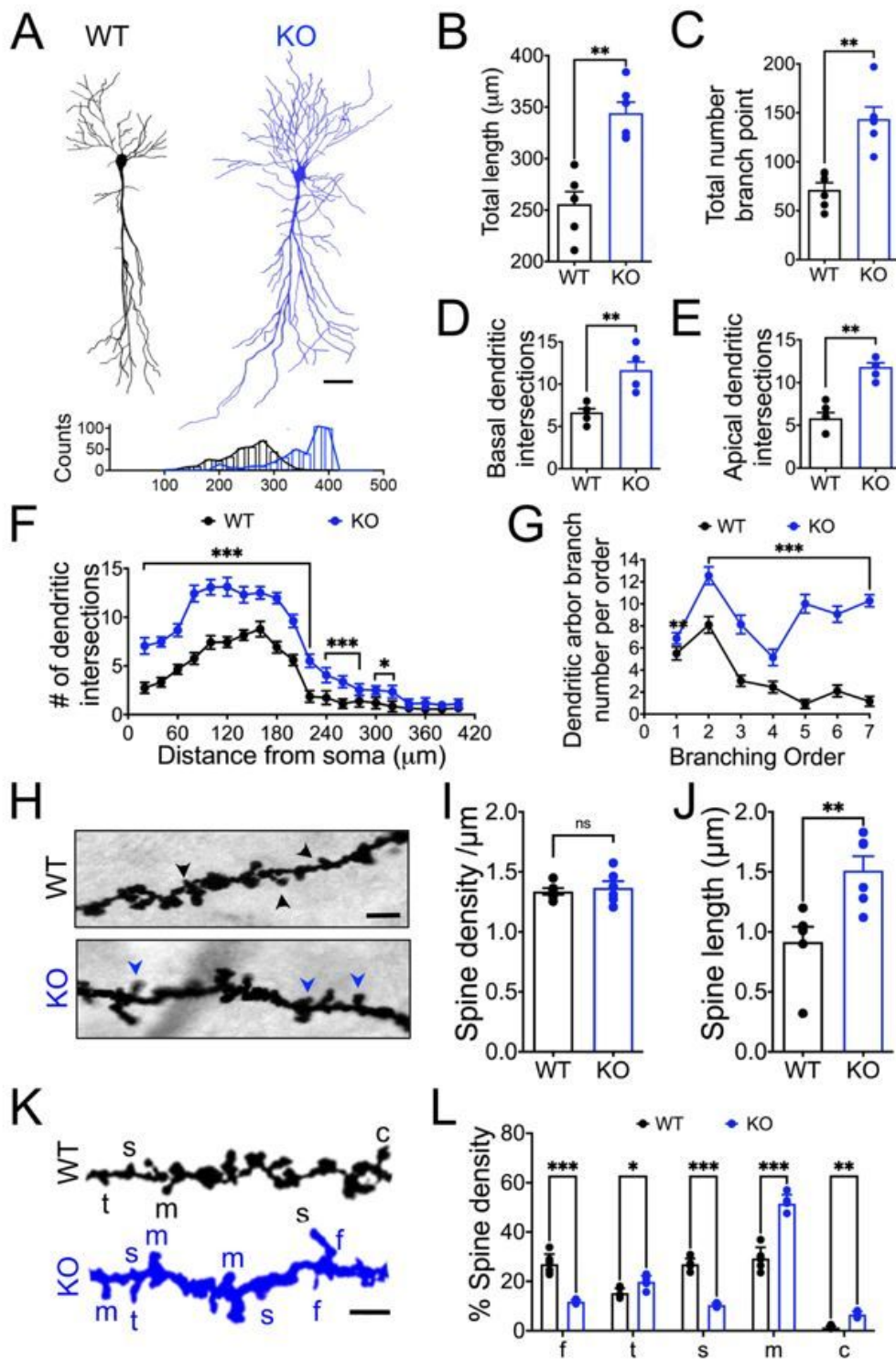


Figure 4

Enhanced dendritic arborization and spine maturation in PANX1-KO neurons. (A) Representative drawings of Golgi stained CA1 neurons (top) and histogram distribution of total dendritic length (bottom) for wild-type (WT, black) and PANX1-knockout (KO, blue) mice (B) Averaged total dendritic length. $n = 6$ (WT) and $n = 6$ (KO) slices from 6 animals, $**p=0.002$ Mann-Whitney test. (C) Averaged basal dendritic branches. $n = 6$ (WT) and $n = 6$ (KO) slices from 6 animals, $**p=0.002$ Mann-Whitney test. (D) Averaged apical

dendritic branches. n = 6 (WT) and n = 6 (KO) slices from 6 animals, **p=0.002 Mann-Whitney test. dendritic branches. **(E)** Averaged dendritic intersections. n = 6 (WT) and n = 6 (KO) slices from 6 animals, **p=0.002 Mann-Whitney test. dendritic branches. **(F)** Number of intersections as a function of the distance from soma. n = 6 (WT) and n = 6 (KO) slices from 6 animals, ****p<0.0001 2way ANOVA test. **(G)** Branch order as a function of the distance from soma. n = 6 (WT) and n = 6 (KO) slices from 6 animals, ***p<0.001 2way ANOVA test. **(H)** Representative images of dendritic segments with dendritic spines (arrowheads). **(I)** Averaged spine density. **(J)** Averaged spine length. n = 6 (WT) and n = 6 (KO) slices from 6 animals, **p=0.004 Mann-Whitney test. **(K)** Pseudo-colored images of dendritic segments as in **(H)** showing different types of dendritic spines, filopodium (f), thin (t), short (s), and mushroom (m) types. Magnification 100X, bar: 50 μ m. **(L)** Proportion of different types of dendritic spines. n = 6 (WT) and n = 6 (KO) slices from 6 animals, *p=0.02, **p=0.005, ***p<0.001 2way ANOVA test.

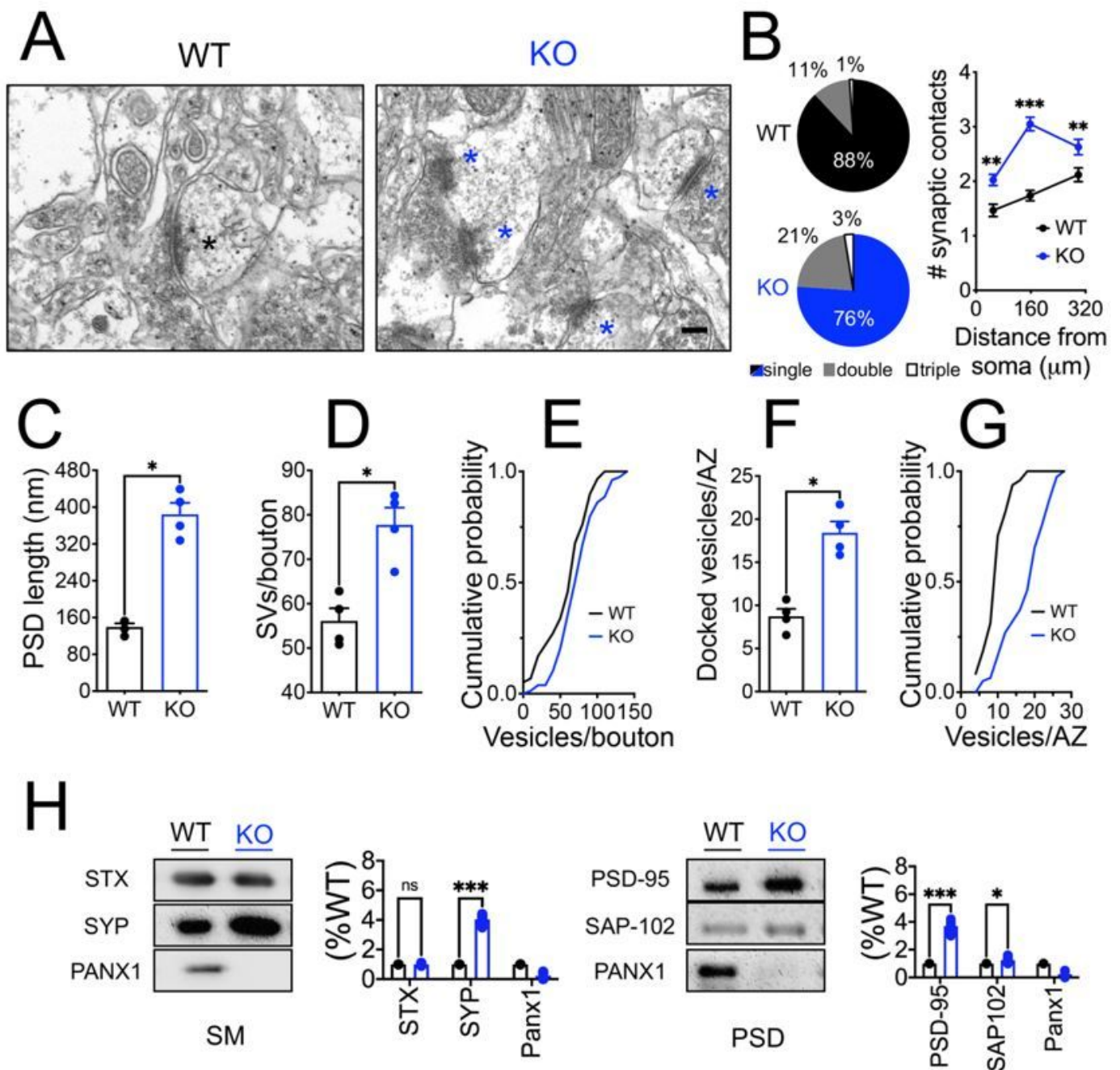


Figure 5

Multiple contacts, higher number of docked vesicles and enhanced PSD length in PANX1-KO synapses.

(A) Representative transmission electron microscopy photographs of asymmetric synapses of CA1 *Stratum radiatum* area of wild-type (WT, black) and PANX1-KO (KO, blue) mice. (B) Percentage of single, double, and triple contacts. $n = 6$ (WT) and $n = 6$ (KO) slices from 3 animals, $**p=0.002$, $****p<0.0001$ 2way ANOVA test. Averaged number of contacts as a function of the distance from soma. $n = 6$ (WT) and $n = 6$ (KO) slices from 3 animals, $*p=0.03$ Mann-Whitney test. (C) PSD length. (D) Number of synaptic vesicles per bouton. $n = 6$ (WT) and $n = 6$ (KO) slices from 3 animals, $*p=0.0286$ Mann-Whitney test. (E)

Cumulative probability of the docked vesicles distribution. **(F)** Number of docked vesicles at the active zone. $n = 6$ (WT) and $n = 6$ (KO) slices from 3 animals, $*p=0.0286$ Mann-Whitney test. **(G)** Cumulative probability of the vesicles/AZ distribution. Magnification 43000X, bar: 500nm. **(H)** Representative blots and densitometric analysis of synaptic proteins levels in PSD-enriched and synaptic membranes avoided of PSD (SM)-enriched fractions. $n = 6$ (WT) and $n = 6$ (KO) slices from 3 animals, $**p=0.002$, $***p<0.0001$ 2way ANOVA test.

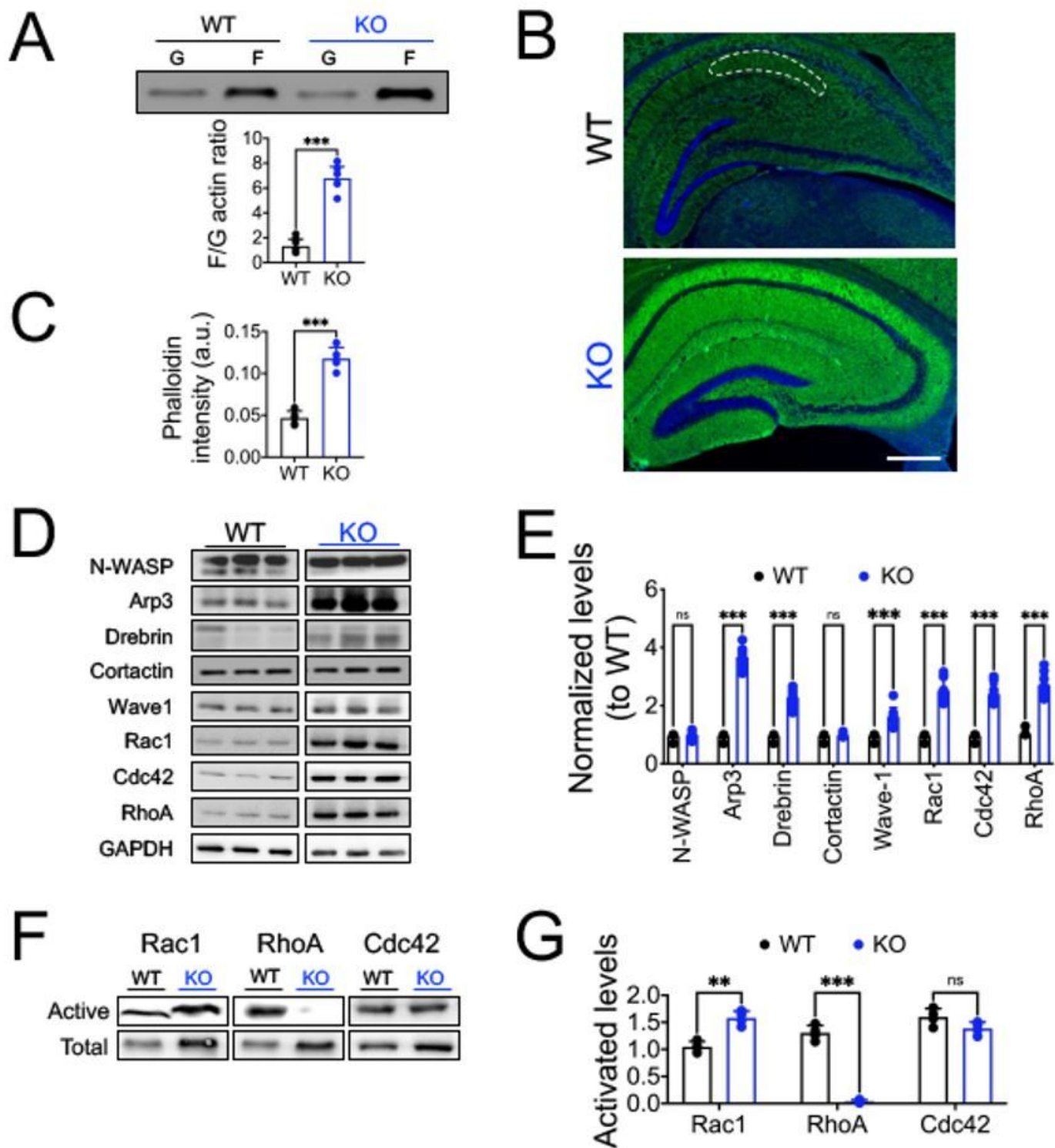


Figure 6

Increased actin polymerization and Rac1 activity in PANX1-KO hippocampi. (A) Representative blots (top) and densitometric analysis of the relative amount of monomers (G) and filaments (F) of actin (bottom), in hippocampal lysates of wild-type (WT, black) and Panx1-KO (KO, blue) mice. (B) Representative micrographs showing Phalloidin-AF488 staining of the F-actin network in the CA1 region in the hippocampus. Scale bar: 50 μ m. (C) Quantification of phalloidin intensity. (D) Representative blots and

densitometric analysis of small Rho GTPases and synaptic actin-binding proteins levels (**E**). (**F**) Representative blots and densitometric analysis of the relative ratios of the active Rac1, Cdc42 and RhoA proteins (**G**). All data are expressed as mean \pm SEM of WT (n = 5) and Panx1-KO (n = 6), *p<0.005, **p<0.001.